

A precision study of two eclipsing white dwarf plus M dwarf binaries

S. G. Parsons^{1*}, T. R. Marsh¹, B. T. Gänsicke¹, A. Rebassa-Mansergas², V. S. Dhillon³, S. P. Littlefair³, C. M. Copperwheat¹, R. D. G. Hickman¹, M. R. Burleigh⁴, P. Kerry³, D. Koester⁵, A. Nebot Gómez-Morán⁶, S. Pyrzas¹, C. D. J. Savoury³, M. R. Schreiber², L. Schmidtobreick⁷, A. D. Schwope⁶, P. R. Steele⁴ and C. Tappert²

¹*Department of Physics, University of Warwick, Coventry, CV4 7AL, UK*

²*Departamento de Física y Astronomía, Universidad de Valparaíso, Avenida Gran Bretaña 1111, Valparaíso, Chile*

³*Department of Physics and Astronomy, University of Sheffield, Sheffield S3 7RH, UK*

⁴*Department of Physics and Astronomy, University of Leicester, Leicester, LE1 7RH, UK*

⁵*Institut für Theoretische Physik und Astrophysik, Universität Kiel, Germany*

⁶*Leibniz-Institut für Astrophysik Potsdam, An der Sternwarte 16, 14482 Potsdam, Germany*

⁷*European Southern Observatory, Alonso de Cordova 3107, Santiago, Chile*

Accepted 2011 November 23. Received 2011 November 23; in original form 2011 October 3

ABSTRACT

We use a combination of X-shooter spectroscopy, ULTRACAM high-speed photometry and SOFI near-infrared photometry to measure the masses and radii of both components of the eclipsing post common envelope binaries SDSS J121258.25-012310.1 and GK Vir. For both systems we measure the gravitational redshift of the white dwarf and combine it with light curve model fits to determine the inclinations, masses and radii. For SDSS J1212-0123 we find an inclination of $i = 85.7^\circ \pm 0.5^\circ$, masses of $M_{\text{WD}} = 0.439 \pm 0.002M_\odot$ and $M_{\text{sec}} = 0.273 \pm 0.002M_\odot$ and radii $R_{\text{WD}} = 0.0168 \pm 0.0003R_\odot$ and $R_{\text{sec}} = 0.306 \pm 0.007R_\odot$. For GK Vir we find an inclination of $i = 89.5^\circ \pm 0.6^\circ$, masses of $M_{\text{WD}} = 0.564 \pm 0.014M_\odot$ and $M_{\text{sec}} = 0.116 \pm 0.003M_\odot$ and radii $R_{\text{WD}} = 0.0170 \pm 0.0004R_\odot$ and $R_{\text{sec}} = 0.155 \pm 0.003R_\odot$. The mass and radius of the white dwarf in GK Vir are consistent with evolutionary models for a 50,000K carbon-oxygen core white dwarf. Although the mass and radius of the white dwarf in SDSS J1212-0123 are consistent with carbon-oxygen core models, evolutionary models imply that a white dwarf with such a low mass and in a short period binary must have a helium core. The mass and radius measurements are consistent with helium core models but only if the white dwarf has a very thin hydrogen envelope ($M_{\text{H}}/M_{\text{WD}} \leq 10^{-6}$). Such a thin envelope has not been predicted by any evolutionary models. The mass and radius of the secondary star in GK Vir are consistent with evolutionary models after correcting for the effects of irradiation by the white dwarf. The secondary star in SDSS J1212-0123 has a radius ~ 9 per cent larger than predicted.

Key words: binaries: eclipsing – stars: fundamental parameters – stars: late-type – white dwarfs

1 INTRODUCTION

Detached eclipsing binaries are a primary source of accurate physical properties of stars and stellar remnants. A combination of modelling their light curves and measur-

ing the radial velocities of both components allows us to measure masses and radii to a precision of better than 1 per cent (e.g. Andersen 1991; Southworth et al. 2005; Southworth et al. 2007; Torres et al. 2010). These measurements are crucial for testing theoretical mass-radius relations, which are used in a wide range of astrophysical circumstances such as inferring accurate masses and radii of

* steven.parsons@warwick.ac.uk

transiting exoplanets, calibrating stellar evolutionary models and understanding the late evolution of mass transferring binaries such as cataclysmic variables (Littlefair et al. 2008; Savoury et al. 2011). Additionally, the mass-radius relation for white dwarfs has played an important role in estimating the distance to globular clusters (Renzini et al. 1996) and the determination of the age of the galactic disk (Wood 1992).

On the one hand, although ubiquitous in the solar neighbourhood, the fundamental properties of low-mass M dwarfs are not as well understood as those of more massive stars (Kraus et al. 2011). There is disagreement between models and observations, consistently resulting in radii up to 15 per cent larger and effective temperatures 400K or more below theoretical predictions (Ribas 2006; López-Morales 2007). These inconsistencies are not only seen in M dwarf eclipsing binaries (Bayless & Orosz 2006; Kraus et al. 2011) but also in field stars (Berger et al. 2006; Morales et al. 2008) and the host stars of transiting extra-solar planets (Torres 2007).

On the other hand, the mass-radius relation for white dwarfs is all but untested observationally. Provençal et al. (1998) used *Hipparcos* parallaxes to determine the radii for white dwarfs in visual binaries, common proper-motion (CPM) systems and field white dwarfs. However, the radius measurements for all of these systems still rely to some extent on model atmosphere calculations. For field white dwarfs the mass determinations are also indirect. Barstow et al. (2005) used *Hubble Space Telescope*/STIS spectra to measure the mass of Sirius B to high precision, however, their radius constraint still relied on model atmosphere calculations and is therefore less direct when it comes to testing white dwarf mass-radius relations. Double white dwarf eclipsing binaries potentially allow extremely precise measurements of white dwarf masses and radii but have only recently been discovered (Steinfeldt et al. 2010; Parsons et al. 2011a; Brown et al. 2011; Vennes et al. 2011b). To date, only a handful of white dwarfs have had their masses and radii model-independently measured, V471 Tau (O’Brien et al. 2001), NN Ser (Parsons et al. 2010a), SDSS J0857+0342 (Parsons et al. 2011b) and SDSS J1210+3347 (Pyrzas et al. 2011). All of these systems are short period post common envelope binaries (PCEBs), demonstrating the potential of these systems for testing mass-radius relations of both low mass stars and white dwarfs.

In this paper we combine X-shooter spectroscopy, ULTRACAM high-speed photometry and SOFI near-infrared photometry to determine precise system parameters for the eclipsing PCEBs SDSS J121258.25-012310.1 (henceforth SDSS J1212-0123) (Nebot Gómez-Morán et al. 2009) and GK Vir (Green et al. 1978). We then compare our mass and radius measurements with theoretical mass-radius relations for white dwarfs and low-mass stars.

2 OBSERVATIONS AND THEIR REDUCTION

2.1 ULTRACAM photometry

GK Vir and SDSS J1212-0123 were observed with ULTRACAM mounted as a visitor instrument on the 3.5m New

Technology Telescope (NTT) at La Silla in April 2010. ULTRACAM is a high-speed, triple-beam CCD camera (Dhillon et al. 2007) which can acquire simultaneous images in three different bands; for our observations we used the SDSS u' , g' and i' filters. A complete log of these observations is given in Table 1. The data collected for GK Vir were combined with previous observations of the system taken with ULTRACAM (see Parsons et al. 2010b for details of these observations). We windowed the CCD in order to achieve exposure times of ~ 3 seconds which we varied to account for the conditions. The dead time between exposures was ~ 25 ms.

All of these data were reduced using the ULTRACAM pipeline software. Debiassing, flatfielding and sky background subtraction were performed in the standard way. The source flux was determined with aperture photometry using a variable aperture, whereby the radius of the aperture is scaled according to the full width at half maximum (FWHM). Variations in observing conditions were accounted for by determining the flux relative to a comparison star in the field of view. Apparent magnitudes and coordinates for each of the comparison stars used are given in Table 2. We flux calibrated our targets by determining atmospheric extinction coefficients in each of the bands in which we observed and calculated the absolute flux of our targets using observations of standard stars (from Smith et al. 2002) taken in twilight. Using our absorption coefficients we extrapolated all fluxes to an airmass of 0. The systematic error introduced by our flux calibration is < 0.1 mag in all bands.

2.2 SOFI J -band photometry

We observed both GK Vir and SDSS J1212-0123 with SOFI (Moorwood et al. 1998) mounted at the NTT in April 2010 and April 2011. The observations were made in fast photometry mode equipped with a J -band filter. We windowed the detector to achieve a cycle time of ~ 10 – 15 seconds and offset the telescope every 10 minutes in order to improve sky subtraction. A summary of these observations is given in Table 1.

The dark current removal (which also removes the bias) and flatfielding were performed in the standard way. Sky subtraction was achieved by using observations of the sky when the target had been offset. The average sky level was then added back so that we could determine the source flux and its uncertainty with standard aperture photometry, using a variable aperture, within the ULTRACAM pipeline. A comparison star was used to account for variations in observing conditions, details of these are given in Table 2. Flux calibration was done using the comparison star J -band magnitude retrieved from the 2MASS catalogue (Skrutskie et al. 2006).

2.3 X-shooter spectroscopy

GK Vir and SDSS J1212-0123 were both observed with X-shooter (D’Odorico et al. 2006) mounted at the VLT-UT2 telescope on the night of the 4th of April 2010. Due to the long orbital periods of both systems (~ 8 hours) we targeted the quadrature phases, since these phases are the most sensitive to the radial velocity amplitude. Conditions through-

Table 1. Journal of observations. Exposure times for X-shooter observations are for UVB arm, VIS arm and NIR arm respectively. The primary eclipse occurs at phase 1, 2 etc.

Date at start of run	Target	Instrument	Filter(s)	Start (UT)	Orbital phase	Exposure time (s)	Conditions (Transparency, seeing)
2010/04/05	SDSS J1212-0123	X-shooter	-	00:42	0.57–0.79	300,338,100	Excellent, ~ 1 arcsec
2010/04/05	GK Vir	X-shooter	-	04:28	0.12–0.26	300,338,100	Excellent, ~ 1 arcsec
2010/04/05	SDSS J1212-0123	X-shooter	-	05:57	0.23–0.45	300,338,100	Excellent, ~ 1 arcsec
2010/04/05	GK Vir	X-shooter	-	07:55	0.53–0.75	300,338,100	Good, ~ 1.2 arcsec
2010/04/21	GK Vir	ULTRACAM	$u'g'i'$	07:18	0.90–1.05	3.0	Good, ~ 1.2 arcsec
2010/04/22	SDSS J1212-0123	ULTRACAM	$u'g'i'$	02:26	0.40–0.55	2.9	Good, ~ 1.2 arcsec
2010/04/22	GK Vir	ULTRACAM	$u'g'i'$	04:14	0.45–0.55	3.0	Excellent, ~ 1 arcsec
2010/04/23	SDSS J1212-0123	ULTRACAM	$u'g'i'$	02:46	0.40–0.55	2.9	Excellent, < 1 arcsec
2010/04/23	GK Vir	ULTRACAM	$u'g'i'$	04:45	0.40–0.55	3.0	Excellent, < 1 arcsec
2010/04/24	SDSS J1212-0123	ULTRACAM	$u'g'i'$	22:57	0.90–1.15	2.9	Good, ~ 1.2 arcsec
2010/04/25	GK Vir	ULTRACAM	$u'g'i'$	06:29	0.40–0.55	3.0	Variable, 1–2 arcsec
2010/04/29	GK Vir	SOFI	J	01:16	0.40–0.55	15.0	Excellent, < 1 arcsec
2010/04/30	GK Vir	SOFI	J	02:17	0.45–0.60	15.0	Good, ~ 1.2 arcsec
2010/04/30	SDSS J1212-0123	SOFI	J	03:56	0.40–0.55	10.0	Excellent, ~ 1 arcsec
2010/04/30	GK Vir	SOFI	J	06:16	0.90–1.05	15.0	Excellent, ~ 1 arcsec
2010/05/01	GK Vir	SOFI	J	02:42	0.40–0.55	15.0	Good, ~ 1.2 arcsec
2011/04/02	SDSS J1212-0123	SOFI	J	01:07	0.43–0.56	10.0	Excellent, < 1 arcsec
2011/04/02	GK Vir	SOFI	J	04:05	0.38–0.59	15.0	Excellent, < 1 arcsec
2011/04/02	GK Vir	SOFI	J	08:02	0.86–1.05	15.0	Excellent, < 1 arcsec
2011/04/03	SDSS J1212-0123	SOFI	J	01:04	0.40–0.61	10.0	Excellent, ~ 1 arcsec
2011/04/03	GK Vir	SOFI	J	05:03	0.40–0.61	15.0	Excellent, ~ 1 arcsec
2011/04/04	SDSS J1212-0123	SOFI	J	01:34	0.44–0.62	10.0	Excellent, ~ 1 arcsec
2011/04/04	GK Vir	SOFI	J	05:33	0.37–0.66	15.0	Excellent, ~ 1 arcsec
2011/04/05	SDSS J1212-0123	SOFI	J	01:04	0.35–0.57	10.0	Excellent, ~ 1 arcsec
2011/04/05	GK Vir	SOFI	J	05:56	0.95–1.20	15.0	Excellent, ~ 1 arcsec
2011/04/05	SDSS J1212-0123	SOFI	J	05:06	0.85–1.06	10.0	Excellent, ~ 1 arcsec
2011/04/05	GK Vir	SOFI	J	06:53	0.43–0.69	15.0	Excellent, ~ 1 arcsec
2011/04/06	SDSS J1212-0123	SOFI	J	01:54	0.43–0.60	10.0	Excellent, < 1 arcsec
2011/04/06	GK Vir	SOFI	J	03:19	0.90–1.17	15.0	Excellent, < 1 arcsec
2011/04/06	SDSS J1212-0123	SOFI	J	05:59	0.94–1.12	10.0	Excellent, < 1 arcsec
2011/04/06	GK Vir	SOFI	J	07:32	0.42–0.62	15.0	Excellent, < 1 arcsec

Table 2. Comparison star apparent magnitudes and coordinates. Magnitudes listed are for those bands for which the comparison star was used.

Target star	Comp RA	Comp Dec	u'	g'	i'	J
GK Vir	14:15:22.86	+01:19:12.7	14.5	13.5	13.1	-
SDSS J1212-0123	12:12:54.97	-01:20:25.0	13.8	12.5	11.9	-
GK Vir	14:15:29.31	+01:17:37.9	-	-	-	13.7
SDSS J1212-0123	12:13:00.51	-01:23:23.3	-	-	-	13.4

out the night were excellent with seeing consistently below 1 arcsec. Details of these observations are listed in Table 1.

X-shooter is a medium resolution spectrograph consisting of 3 independent arms that give simultaneous spectra longward of the atmospheric cutoff (0.3 microns) in the UV (the “UVB” arm), optical (the “VIS” arm) and up to 2.5 microns in the near-infrared (the “NIR” arm). We used slit widths of 0.8”, 0.9” and 0.9” in X-shooter’s three arms and binned by a factor of two in the dispersion direction, resulting in a resolution of $R \sim 7,000$. We used exposure times of 300 seconds in the UVB arm, 338 seconds in the VIS arm and 3×100 seconds in the NIR arm. After each exposure we nodded along the slit to help the sky subtraction in the NIR arm.

The reduction of the raw frames was conducted us-

ing the standard pipeline release of the X-shooter Common Pipeline Library (CPL) recipes (version 1.3.7) within ES-ORex, the ESO Recipe Execution Tool, version 3.9.0. The standard recipes were used to optimally extract and wavelength calibrate each spectrum. For the NIR arm we combined frames taken at different nod positions to improve the sky subtraction, however, this does result in a reduction in orbital phase resolution. The instrumental response was removed by observing the spectrophotometric standard star GJ 440 and dividing it by a flux table of the same star (Hamuy et al. 1992) to produce the response function, this was also used to apply a telluric correction to the spectra. We then heliocentrically corrected the wavelength scales of each of the spectra. We achieved a signal-to-noise (S/N) for GK Vir of ~ 20 in the UVB arm per exposure, ~ 15 in the

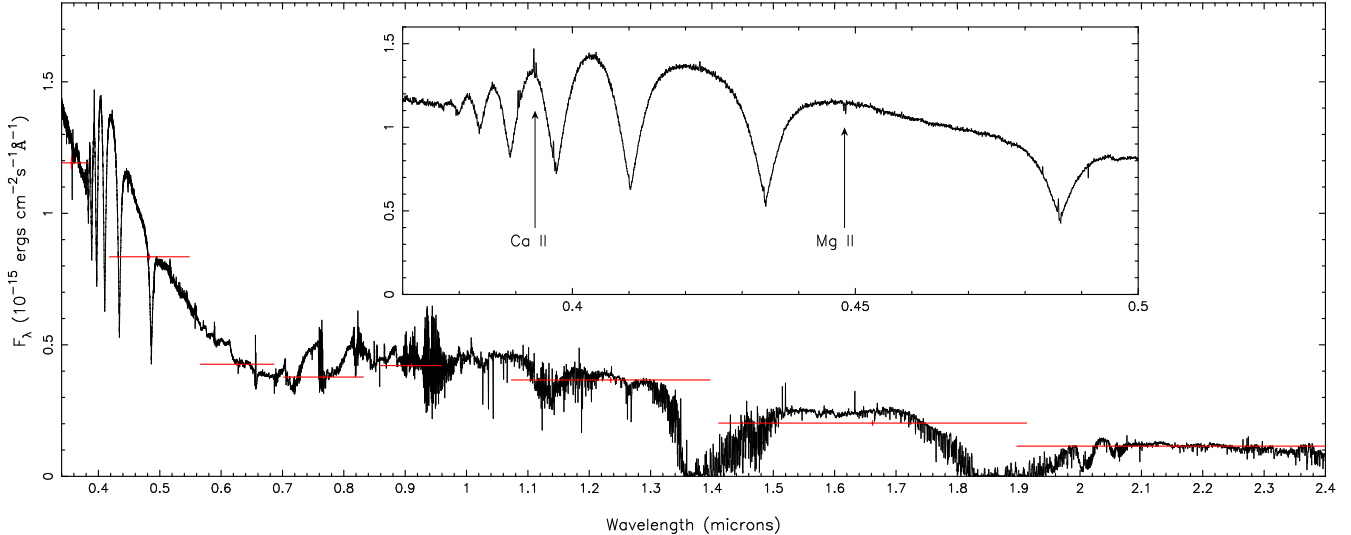


Figure 1. Averaged X-shooter spectrum of SDSS J1212-0123. The SDSS $u'g'r'i'z'$ and 2MASS JHK magnitudes and filter widths are also shown. A zoom in on the white dwarf features are shown inset with the narrow Ca II and Mg II absorption features labelled, although the Ca II feature is somewhat filled in by emission from the secondary star.

VIS arm per exposure and ~ 5 in the NIR arm per pair of nodded exposures. For SDSS J1212-0123 we achieved a S/N of ~ 20 in the UVB arm per exposure, ~ 30 in the VIS arm per exposure and ~ 20 in the NIR arm per pair of nodded exposures.

2.4 Flux calibration

The ULTRACAM and SOFI light curves were used to flux calibrate the X-shooter spectra. We fitted a model to each of the light curves (see Section 3.1.8) in order to reproduce the light curve as closely as possible. The model was then used to predict the flux at the times of each of the X-shooter observations (GK Vir shows no stochastic variations or flaring, whilst small flares were seen in one ULTRACAM observation and two SOFI observations of SDSS J1212-0123 but were removed before fitting).

We then derived synthetic fluxes from the spectra for the ULTRACAM u' , g' , r' , i' and z' filters as well as the SOFI J , H and K filters. We extrapolated the light curve models to those bands not covered by our photometry. We then calculated the difference between the model and synthetic fluxes and fitted a second-order polynomial to them. This correction was then applied to each spectrum. This corrects for variable extinction across the wavelength range, as well as variations in seeing.

3 RESULTS

3.1 SDSS J1212-0123

SDSS J1212-0123 was initially listed as a quasar candidate from the Sloan Digital Sky Survey (SDSS) by Richards et al. (2004). Silvestri et al. (2006) reclassified it as a white dwarf plus main-sequence binary and eclipses were discovered by Nebot Gómez-Morán et al. (2009) who derived the basic system parameters. However, their analysis was limited by the fact that they did not resolve the white dwarf ingress

or egress and could not measure the radial velocity amplitude of the white dwarf. They found that SDSS J1212-0123 contained a relatively hot ($17,700 \pm 300\text{K}$) low mass white dwarf with an active M4 main-sequence companion in an $8^{\text{h}}3^{\text{m}}$ period.

3.1.1 Spectral features

Figure 1 shows an average spectrum of SDSS J1212-0123. The white dwarf dominates the spectrum at wavelengths shorter than 0.55 microns whilst at longer wavelengths the spectral features of the secondary star dominate. There are also numerous emission lines throughout the spectrum originating from the secondary star. Additionally, both Ca II 3934Å and Mg II 4481Å absorption from the white dwarf are seen, likely the result of low level accretion from the wind of the secondary star. The fact that absorption features are seen from both stars allows us to measure the radial velocities for both components of the system directly.

3.1.2 Atmospheric parameters of the white dwarf

Nebot Gómez-Morán et al. (2009) determined the temperature of the white dwarf in SDSS J1212-0123 by decomposing the SDSS spectrum. We computed the average X-shooter spectrum of the white dwarf by removing the M-dwarf contribution from the individual spectra using observations of the M4 star GJ 447, and shifting the residual spectra to the rest frame of the white dwarf, however this does not remove the emission components. We then fit the average white dwarf spectrum following the method outlined in Rebassa-Mansergas et al. (2007, 2010), using a grid of pure hydrogen model atmospheres calculated with the code described by Koester (2010). We down-weight the cores of the Balmer lines since they are contaminated by emission from the secondary star, we do not use the H α line since the secondary star dominates at this wavelength, all other lines were used. We find a temperature of $17,707 \pm 35\text{K}$,

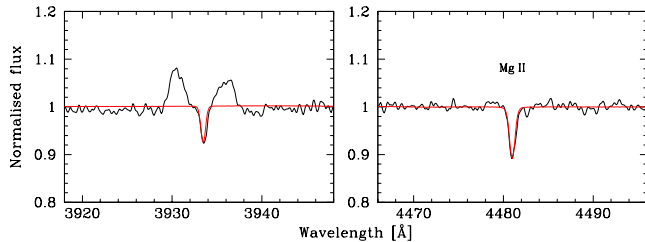


Figure 2. The X-shooter spectra of SDSS J1212-0123, averaged in the white dwarf rest-frame and normalised (black) along with the best-fit white dwarf model ($T_{\text{eff}} = 17707$, $\log g = 7.51$) and $\log[\text{Mg}/\text{H}] = -5.8$. The Ca K line is contaminated by the emission from the secondary star (which appears shifted/smearred in the rest frame of the white dwarf), however, adopting the same abundance for Ca provides a reasonable match to the photospheric absorption line.

a surface gravity of $\log g = 7.51 \pm 0.01$ and a distance of $228 \pm 5 \text{ pc}$, all of which is consistent with the results from Nebot Gómez-Morán et al. (2009) (and from our light curve fit, see Section 4). Note that these are purely statistical uncertainties.

Next, we fitted the equivalent width of the observed Mg II 4481 Å absorption line ($90 \pm 20 \text{ mÅ}$) by varying the Mg abundance in the synthetic spectrum, keeping T_{eff} and $\log g$ fixed to the values determined above. The best-fit abundance by number is $\log[\text{Mg}/\text{H}] = -5.8 \pm 0.1$, corresponding to $\simeq 4\%$ of the solar value. Figure 2 shows the fit to the Mg II 4481 Å line. The Ca K line is significantly contaminated by the emission line of the companion star, however, Figure 2 illustrates that adopting the Mg abundance also for Ca matches the observed Ca K line reasonably well.

Since there is no convection zone acting as a reservoir for the accreted elements, the settling times vary throughout the atmosphere. At optical depth $\sim 2/3$, representative for the visible spectrum, the timescale for Mg is a few tens of days. The diffusion time scale for the temperature and surface gravity derived above is ~ 2 months (Koester & Wilken 2006), it is hence plausible to assume accretion-diffusion equilibrium. Hence, $X_{\text{Mg}}\rho v_{\text{Mg}} = \text{constant}$, with X_{Mg} and v_{Mg} the mass fraction and the diffusion velocity (relative to hydrogen) of Mg, and ρ the mass density. We compute at $\tau_{\text{Ross}} \approx 2/3$ $\rho = 5.23 \times 10^{-8} \text{ g cm}^{-3}$, $X_{\text{Mg}} = 3.76 \times 10^{-5}$, and $v_{\text{Mg}} = 8.48 \times 10^{-2} \text{ cm s}^{-1}$, i.e. a mass flux of $1.67 \times 10^{-13} \text{ g cm}^{-2} \text{ s}^{-1}$. Multiplying by the white dwarf surface area, with R_{WD} from Table 9, the total mass flux of Mg is $2.9 \times 10^6 \text{ g s}^{-1}$ – which is equal to the mass accretion rate of Mg at the surface of the white dwarf. Assuming that the donor star transfers material of solar composition, the total accretion rate is then obtained by dividing the Mg rate by the mass fraction of Mg in the Sun, i.e. $\dot{M} \simeq 4.0 \times 10^9 \text{ g s}^{-1}$ or $6.4 \times 10^{-17} M_{\odot} \text{ yr}^{-1}$. This value is right in the middle of the accretion rates calculated for the pre-CVs RR Cae, UZ Sex, EG UMa, LTT 560 and SDSS J121010.1+334722.9 by Debes (2006), Tappert et al. (2011), and Pyrzas et al. (2011), $9 \times 10^{-19} M_{\odot} \text{ yr}^{-1}$ to $5 \times 10^{-15} M_{\odot} \text{ yr}^{-1}$.

Table 3. White dwarf absorption features in SDSS J1212-0123.

Line	K_{WD} (km s^{-1})	γ_{WD} (km s^{-1})
Ca II 3933.663	102.71 ± 1.32	37.36 ± 1.12
H δ 4101.735	106.22 ± 2.21	35.14 ± 1.85
H γ 4340.465	104.28 ± 1.24	37.43 ± 1.08
Mg II 4481.126	104.53 ± 0.78	35.75 ± 0.67
H β 4861.327	105.49 ± 0.93	35.25 ± 0.42
H α 6562.760	103.32 ± 1.13	38.66 ± 0.97

3.1.3 White dwarf radial velocity

The orbital phases of the X-shooter spectra of SDSS J1212-0123 were determined using the ephemeris derived in Section 3.1.6. As previously mentioned both Ca II and Mg II absorption from the white dwarf are present. Additionally, the cores of the longer wavelength hydrogen absorption lines (H δ to H α) are narrow and suitable for radial velocity measurements.

We measured the radial velocities of the absorption lines by simultaneously fitting all of the spectra. We used a combination of a straight line and Gaussians for each spectrum (including a broad Gaussian component to account for the wings of the absorption in the case of the Balmer lines) and allowed the position of the Gaussians to change velocity according to

$$V = \gamma + K \sin(2\pi\phi),$$

for each star, where γ is the velocity offset of the line from its rest wavelength and ϕ is the orbital phase of the spectrum.

The parameters determined from the fits to the white dwarf absorption features are listed in Table 3. The fits to several of the absorption features are also shown in Figure 3, the fit to the H α line is also shown in Figure 4. Taking a weighted average of the radial velocities gives a radial velocity amplitude of the white dwarf of $K_{\text{WD}} = 104.4 \pm 0.5 \text{ km s}^{-1}$.

3.1.4 Secondary star radial velocity

There are both absorption and emission features originating from the secondary star seen in the X-shooter spectra. However, the emission features are due to irradiation from the white dwarf hence they do not track the true radial velocity of the secondary star but the centre of light of the emission region, which will be offset towards the white dwarf. Therefore we can only directly measure the velocity amplitude for the secondary star via the absorption lines.

Sodium and Potassium absorption lines are present in the spectra which we fitted in the same way as the white dwarf absorption features. The result of these fits are given in Table 4. There were also a number of molecular absorption features which we do not fit due to the uncertainty in their rest wavelengths and their broad, non-Gaussian profiles. Other atomic absorption features are seen at longer wavelengths (for example: the Na I doublet at 2.2 microns) but the S/N of these features are too low to reliably fit them. A weighted average of the radial velocities of the lines in Table 4 gives a radial velocity amplitude of the secondary star of $K_{\text{sec}} = 168.3 \pm 0.3 \text{ km s}^{-1}$. This is some-

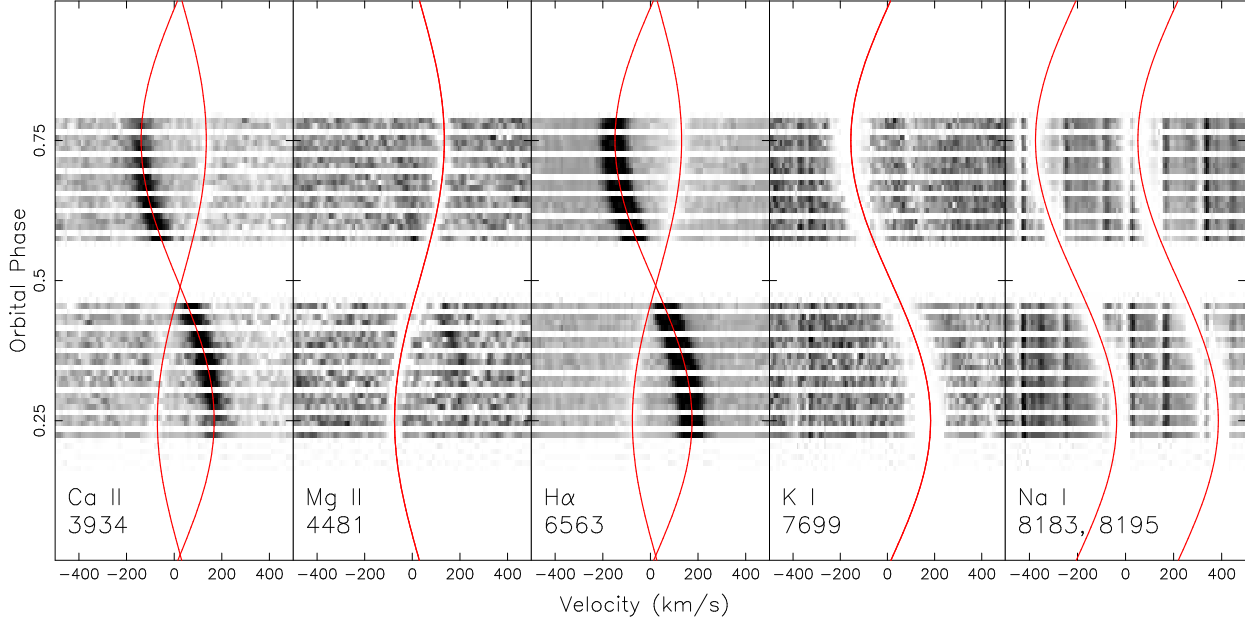


Figure 3. Triled spectra of several lines in SDSS J1212-0123. The grey-scale runs from white (75 per cent of the continuum level) to black (125 per cent of the continuum level). The Ca II 3934Å line shows an absorption component from the white dwarf and an emission component from the M star. The Mg II 4481Å line is from the white dwarf, a weak Fe I emission line is also visible. H α shows both absorption from the white dwarf and emission from the M dwarf. The K I absorption line and the Na I absorption doublet originate from the M star, a telluric correction was applied but artifacts still remain in the Na I trail. The red lines (online version only) show the best fits to the lines.

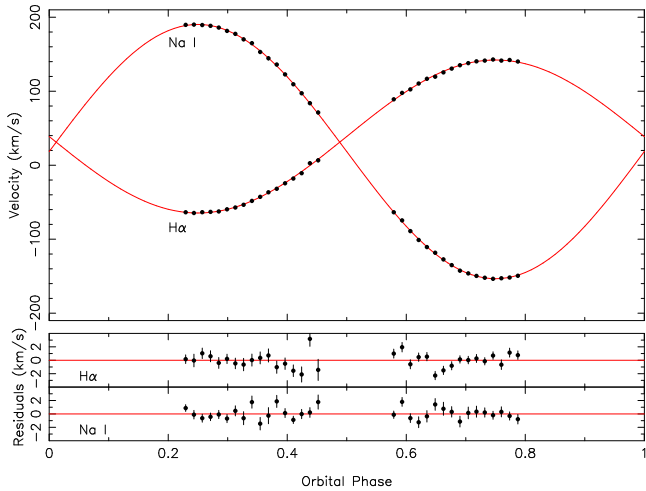


Figure 4. Radial velocity fits to the H α absorption from the white dwarf and Na I 8183Å absorption from the secondary star in SDSS J1212-0123 with residuals plotted below.

what lower than the value of $K_{\text{sec}} = 181 \pm 3 \text{ km s}^{-1}$ found by Nebot Gómez-Morán et al. (2009). To try and resolve this difference we re-fitted the radial velocity data from Nebot Gómez-Morán et al. (2009) and found a $\chi^2 = 25$ for 10 points with 2 variables, implying that they slightly underestimated their error. Accounting for this, their value is consistent with ours to within 2.5σ but, based on our higher resolution and additional clean features (not affected by telluric absorption), we favour our value for K_{sec} . We find no

Table 4. Secondary star atomic absorption features in SDSS J1212-0123. There are several additional atomic absorption features in the NIR arm spectra but the S/N of these lines are too low to reliably fit them.

Line	K_{sec} (km s^{-1})	γ_{sec} (km s^{-1})
K I 7664.899	169.36 ± 1.13	18.27 ± 0.97
K I 7698.964	169.04 ± 0.83	19.28 ± 0.71
Na I 8183.256	168.77 ± 0.45	18.44 ± 0.38
Na I 8194.824	167.42 ± 0.48	19.52 ± 0.41
Na I 11381.45	165.24 ± 3.86	21.51 ± 3.21
Na I 11403.78	166.87 ± 1.20	19.14 ± 1.07
K I 11690.219	170.22 ± 1.37	20.86 ± 1.24
K I 12432.274	168.63 ± 1.01	19.47 ± 0.88
K I 12522.141	167.40 ± 1.03	21.48 ± 0.72

evidence that the absorption lines are affected by irradiation from the white dwarf. The equivalent widths of these lines do not vary with phase and no effects are visible in the radial velocity curves.

We also measured the radial velocity amplitudes of all of the identified emission lines. However, for these lines we allow the height of the emission line to vary with orbital phase according to

$$H = H_0 - H_1 \cos(2\pi\phi),$$

which allows the height to peak at phase 0.5, where the irradiation effect is largest. This approach gives better fits than keeping the height at a fixed value.

The results of these fits are given in Table A1, in the appendix. We find that the emission lines give a range of

Table 5. Eclipse times for SDSS J1212-0123. (1) Nebot Gómez-Morán et al. (2009), (2) This paper.

Cycle No.	MJD(BTDB) (mid-eclipse)	Reference
0	54104.2092(21)	(1)
122	54145.1854(8)	(1)
125	54146.1929(8)	(1)
205	54173.0628(10)	(1)
410	54241.9170(21)	(1)
1455	54592.9008(14)	(1)
3593	55310.9934268(59)	(2)

radial velocities, likely due to the different optical depths of the lines (Parsons et al. 2010a). Figure 3 shows the fits to the Na I doublet as well as several emission lines. The fit to the Na I 8183Å line is shown in Figure 4.

3.1.5 White dwarf’s gravitational redshift

General relativity tells us that the gravitational redshift of a white dwarf is given by

$$V_z = 0.635(M/M_\odot)(R_\odot/R) \text{ km s}^{-1} \quad (1)$$

where M and R are the mass and radius of the white dwarf. Furthermore, if we know the radial velocity amplitudes of the two stars then Kepler’s third law tells us

$$M_{\text{WD}} = \frac{PK_{\text{sec}}(K_{\text{WD}} + K_{\text{sec}})^2}{2\pi G \sin^3 i} \quad (2)$$

where P is the orbital period, and i is the orbital inclination. Therefore for a given inclination we can calculate the mass of the white dwarf via Eq (2) and the radius of the white dwarf via a model fitted to the primary eclipse, and thus predict a redshift. Hence we can use the measurement of the gravitational redshift to constrain the inclination by rejecting light curve models which do not satisfy this constraint.

The gravitational redshift can be measured from the difference in the velocities of the two components ($\gamma_{\text{WD}} - \gamma_{\text{sec}}$). γ_{sec} is tightly constrained due to the large number of emission lines as well as many absorption features. Taking an inverse variance weighted mean of the secondary star line velocities (from Tables 4 and A1) we found $\gamma_{\text{sec}} = 19.93 \pm 0.06 \text{ km s}^{-1}$. We calculated γ_{WD} in the same way using the values in Table 3 which gave $\gamma_{\text{WD}} = 36.0 \pm 0.3 \text{ km s}^{-1}$. We found no evidence of pressure shifts in these lines, although these are expected to be small for calcium and magnesium (Vennes et al. 2011a).

Using these measurements we determined the gravitational redshift of the white dwarf to be $V_z = 16.1 \pm 0.3 \text{ km s}^{-1}$. The true gravitational redshift of the white dwarf will actually be slightly higher than this value since the measured value includes the effects of the secondary star (see Section 3.1.8 for details of these corrections).

3.1.6 Eclipse time

We recorded one eclipse of SDSS J1212-0123 with ULTRACAM. This provides the first high-precision eclipse time for this system. The SOFI eclipses are not suitable for long term period studies as they are not precisely timed. The eclipse

time, as well as all previous eclipse times, are listed in Table 5. The new time is consistent with the ephemeris of Nebot Gómez-Morán et al. (2009) but since it is of higher precision we use it to update the ephemeris to

$$\text{MJD(BTDB)} = 54104.20917(48) + 0.33587093(13)E,$$

where we have used barycentric dynamical time (TDB) corrected for the light travel time to the barycentre of the solar system (BTDB). Since this is the first precise eclipse time, no long-term period trend is yet visible in the data.

3.1.7 Spectral type of the secondary star

From their spectral decomposition Nebot Gómez-Morán et al. (2009) determined the spectral type of the secondary star in SDSS J1212-0123 to be $M4 \pm 1$. We detect the secondary star during the eclipse in all bands except the u' band giving us multi-colour information. We measure magnitudes for the secondary star of $g' = 19.73 \pm 0.04$, $i' = 17.384 \pm 0.004$ and $J = 14.949 \pm 0.001$. The $i' - J = 2.435 \pm 0.004$ colour implies a spectral type of M4 for the secondary star (Hawley et al. 2002, Table 3), consistent with the result from Nebot Gómez-Morán et al. (2009). The distance determined from the spectroscopic fit ($228 \pm 5 \text{ pc}$) means that the absolute J band magnitude of the secondary star is $M_J = 8.2$. Using the M_J -spectral type relation from Hawley et al. (2002), also gives a spectral type of M4.

3.1.8 Modelling the light curves

The light curves of SDSS J1212-0123 are characterised by a deep eclipse of the white dwarf (which gets shallower in the longer wavelength bands). There is little variation out of eclipse and we found no evidence of a secondary eclipse in any of the light curves.

We fitted all of our photometry (for both SDSS J1212-0123 and GK Vir) using a code written to produce models for the general case of binaries containing a white dwarf (see Copperwheat et al. 2010 for details). It has been used in the study of other white dwarf-main sequence binaries (Pyrzas et al. 2009; Parsons et al. 2010a). The program subdivides each star into small elements with a geometry fixed by its radius as measured along the direction of centres towards the other star. Roche geometry distortion and irradiation of the secondary star are included, the irradiation is approximated by $\sigma T'_{\text{sec}}{}^4 = \sigma T_{\text{sec}}{}^4 + AF_{\text{irr}}$ where T'_{sec} is the modified temperature and T_{sec} is the temperature of the unirradiated main-sequence star, σ is the Stefan-Boltzmann constant, A is the fraction of the irradiating flux from the white dwarf absorbed by the secondary star and F_{irr} is the irradiating flux, accounting for the angle of incidence and distance from the white dwarf.

The parameters needed to define the model were: the mass ratio, $q = M_{\text{sec}}/M_{\text{WD}}$, the inclination, i , the sum of the unprojected stellar orbital speeds $V_s = (K_{\text{WD}} + K_{\text{sec}})/\sin(i)$, the stellar radii scaled by the orbital separation R_{sec}/a and R_{WD}/a , the unirradiated temperatures, $T_{\text{eff,WD}}$ and $T_{\text{eff,sec}}$, quadratic limb darkening coefficients for the both stars, the time of mid eclipse, T_0 and the period, P . Note that the temperatures are really just flux scaling parameters and only approximately correspond to the actual temperatures.

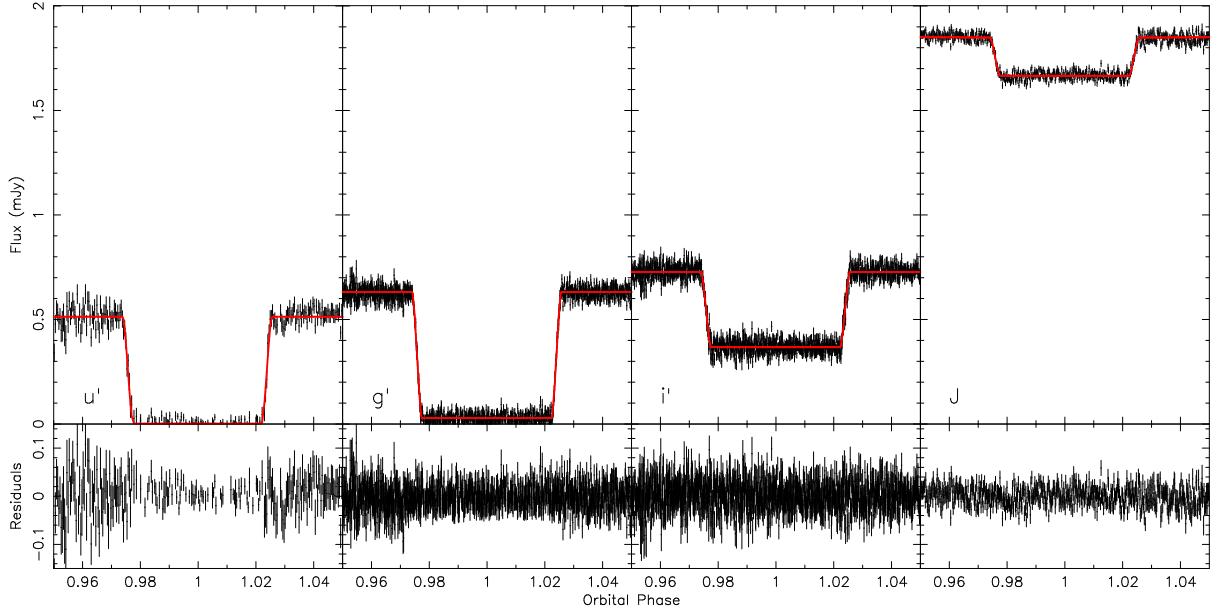


Figure 5. ULTRACAM u' , g' and i' and SOFI J band primary eclipses of SDSS J1212-0123 with model fits and residuals.

Table 6. Parameters from Markov chain Monte Carlo minimisation for SDSS J1212-0123, some fitted, some fixed a priori (those without quoted uncertainties). a and b are the quadratic limb darkening coefficients. A is the fraction of the irradiating flux from the white dwarf absorbed by the secondary star.

Parameter	u'	g'	i'	J
i (deg)	86.1 ± 2.2	85.7 ± 0.6	85.8 ± 0.8	85.5 ± 0.8
r_{WD}/a	0.0092 ± 0.0002	0.0092 ± 0.0002	0.0093 ± 0.0002	0.0092 ± 0.0002
r_{sec}/a	0.171 ± 0.016	0.171 ± 0.005	0.170 ± 0.006	0.172 ± 0.006
$T_{\text{eff,sec}}$ (K)	2618 ± 112	2947 ± 26	3009 ± 41	3342 ± 42
a_{WD}	0.2444	0.1340	0.1071	0.0639
b_{WD}	0.2256	0.2899	0.1891	0.1342
a_{sec}	0.5866	0.6720	0.4193	0.0254
b_{sec}	0.2959	0.2660	0.4109	0.4826
A	1.60 ± 0.50	0.81 ± 0.09	0.45 ± 0.03	0.39 ± 0.02

The light curves are only weakly dependent upon q and V_s . However, we can use them, as well as our measurements of the radial velocity amplitudes and the gravitational redshift of the white dwarf, to help constrain the orbital inclination. This is done by computing the radial velocity amplitudes via

$$K_{\text{WD}} = (q/(1+q))V_s \sin i \quad (3)$$

$$K_{\text{sec}} = (1/(1+q))V_s \sin i, \quad (4)$$

we can also compute the masses using

$$M = PV_s^3/2\pi G, \quad (5)$$

where M is the total system mass. The individual masses are then

$$M_{\text{WD}} = M/(1+q) \quad (6)$$

$$M_{\text{sec}} = qM_{\text{WD}}. \quad (7)$$

The orbital separation a is then calculated from

$$a = V_s/2\pi P, \quad (8)$$

allowing us to calculate the radii of the two stars. Combining

all these calculations yields the masses and radii of both stars. We can then use these to calculate the gravitational redshifts using

$$V_{z,\text{WD}} = 0.635 \left(\frac{M_{\text{WD}}}{R_{\text{WD}}} + \frac{M_{\text{sec}}}{a} \right) + \frac{(K_{\text{WD}}/\sin i)^2}{2c} \quad (9)$$

$$V_{z,\text{sec}} = 0.635 \left(\frac{M_{\text{sec}}}{R_{\text{sec}}} + \frac{M_{\text{WD}}}{a} \right) + \frac{(K_{\text{sec}}/\sin i)^2}{2c}, \quad (10)$$

then the value $V_z = V_{z,\text{WD}} - V_{z,\text{sec}}$ is equivalent to the measured redshift from the X-shooter spectra, which takes into account the effects of the secondary star on the measurement of the white dwarf's gravitational redshift. Therefore after we have generated a model we can compute K_{WD} , K_{sec} and V_z from the fitted parameters and either reject or accept that model based on how close they are to the measured values.

We used the Markov Chain Monte Carlo (MCMC) method to determine the distributions of our model parameters (Press et al. 2007). The MCMC method involves making random jumps in the model parameters, with new models being accepted or rejected according to their proba-

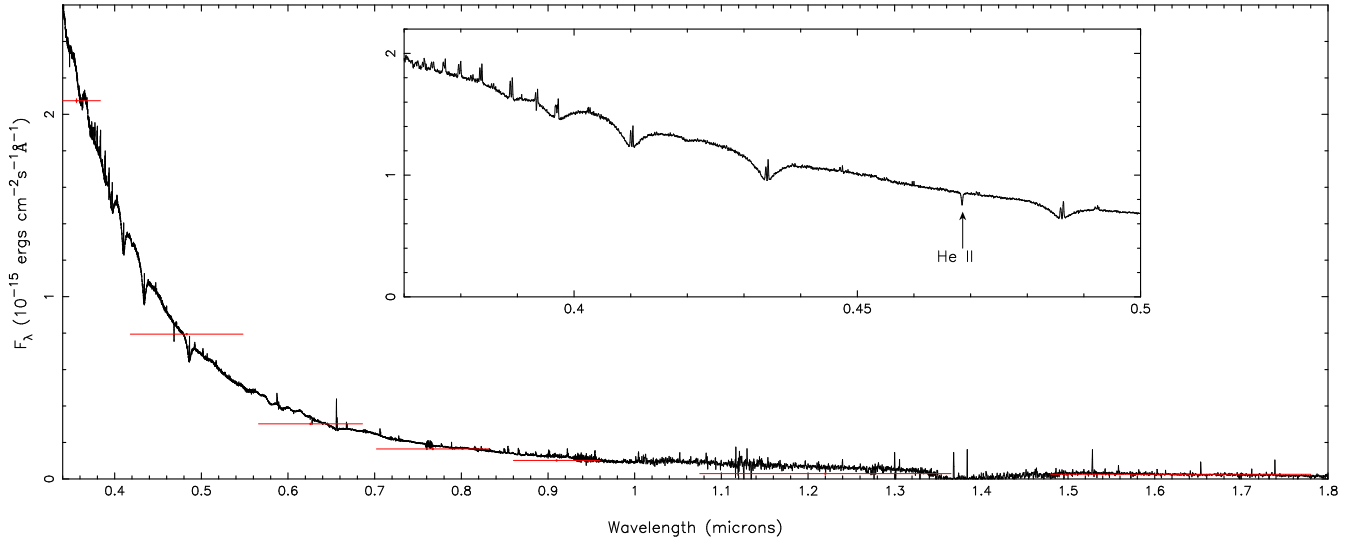


Figure 6. Averaged X-shooter spectrum of GK Vir. The SDSS $u'g'r'i'z'$ and UKIDSS JH magnitudes and filter widths are also shown, the UKIDSS J band observations were made during the primary eclipse. A zoom in on the white dwarf features are shown inset with the narrow He II absorption feature labelled.

bility computed as a Bayesian posterior probability. In this instance this probability is driven by a combination of χ^2 and the prior probability from our spectroscopic constraints (see Parsons et al. 2011b and Pyrzas et al. 2011 for more details of the MCMC fitting process).

For fitting the light curves of SDSS J1212-0123, we phase folded the data and kept the period fixed as one. We also kept the temperature of the white dwarf fixed at 17,900K (see Section 3.1.2). For the secondary star we used quadratic limb darkening coefficients from Claret & Bloemen (2011) for a $T_{\text{eff}} = 3000$, $\log g = 5$ main sequence star. For the white dwarf we calculated quadratic limb darkening coefficients from a white dwarf model with $T_{\text{WD}} = 17,900$ and $\log g = 7.53$ based on our spectroscopic fits, folded through the ULTRACAM u' , g' , i' and SOFI J filter profiles. For both stars we quote the coefficients a and b where $I(\mu)/I(1) = 1 - a(1 - \mu) - b(1 - \mu)^2$, where μ is the cosine of the angle between the line of sight and the surface normal. We kept all limb darkening parameters fixed.

Table 6 lists the best fit parameters from the light curves and their 1σ uncertainties, we also list the limb darkening coefficients used for each band. The results from all four bands are consistent. Figure 5 shows the fits to the primary eclipses in each band and the residuals to the fits.

3.2 GK Vir

GK Vir (PG 1413 + 015) was discovered by Green et al. (1978) from the Palomar-Green survey for ultraviolet-excess objects (Green et al. 1986). An eclipse was recorded during a subsequent spectroscopic observation. Fulbright et al. (1993) combined the photometry from Green et al. (1978) and high resolution spectroscopy to constrain the system parameters. They found that GK Vir contains a hot DAO white dwarf with a low-mass M3-5 main sequence companion in an $8^{\text{h}}16^{\text{m}}$ period. However, their lack of radial velocity information limited their analysis.

3.2.1 Spectral features

Figure 6 shows an average X-shooter spectrum of GK Vir. The hot white dwarf dominates the spectrum at wavelengths shorter than 1 micron. In the J band the secondary star contributes roughly 50 per cent of the overall flux. Hydrogen Balmer absorption lines from the white dwarf are visible as well as narrow He II 4686Å absorption from the white dwarf, making it a DAO white dwarf, as mentioned by Fulbright et al. (1993). Numerous emission lines originating from the heated face of the secondary star are seen throughout the spectrum. Na I (8183Å, 8195Å) absorption originating from the secondary star is seen before phase 0.25 but decreases in strength towards phase 0.5 due to the increased ionisation and therefore cannot be used to measure the radial velocity amplitude of the secondary star. No other absorption features for the secondary star are visible.

3.2.2 Atmospheric parameters of the white dwarf

We fitted the X-Shooter spectrum, averaged in the white dwarf rest-frame, to obtain an estimate of the effective temperature. As for SDSS J1212-0123 (see Section 3.1.2), we fitted the normalised Balmer lines, including H β to H ζ and down-weighting the regions that are noticeably contaminated by emission lines. The best-fit gives a temperature of $55995 \pm 673\text{K}$, a surface gravity of $\log g = 7.68 \pm 0.04$ and a distance of $550 \pm 20\text{pc}$. We note that the quoted errors are purely statistical, and that systematic effects are very likely affecting these results. The X-Shooter data were obtained near the quadrature phases ($\phi \simeq 0.25$ and 0.75 , in order to measure K_{WD} and K_{sec}), which results in a significant contamination by emission from the strongly irradiated inner hemisphere of the secondary star. Varying the wavelength range around the lines that is down-weighted affects the resulting temperature by several 1000 K. For comparison, we also fitted the lower-resolution SDSS spectrum of GK Vir, obtained near superior conjunction of the compan-

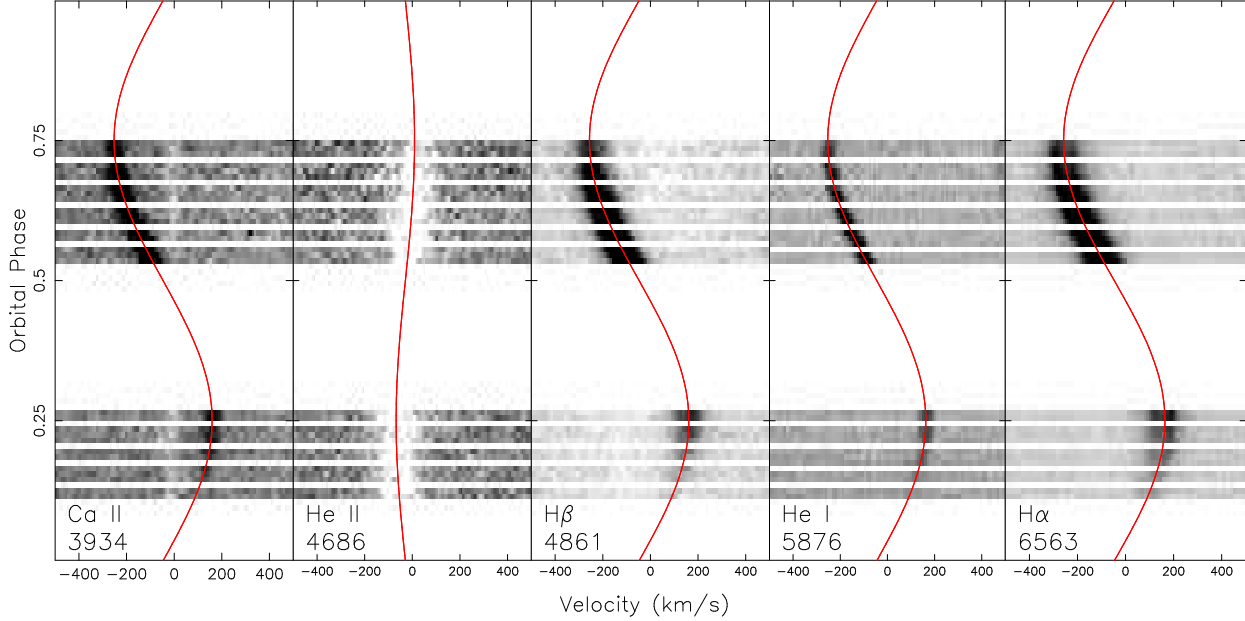


Figure 7. Triled spectra of several lines in GK Vir. The grey-scale runs from white (75 per cent of the continuum level) to black (125 per cent of the continuum level). The Ca II 3934Å line shows emission from the M star as well as weak interstellar absorption which shows no radial velocity variations. The He II 4686Å line originates from the white dwarf. The H β and H α emission from the M star shows inverted cores and asymmetric profiles similar to those seen in NN Ser (Parsons et al. 2010a). The red lines (online version only) show the best fits to the lines.

ion, and find $T_{\text{eff}} = 52258 \pm 3131$ K, $\log g = 7.66 \pm 0.18$, and $d = 509 \pm 61$ pc.

Fulbright et al. (1993) analysed a blue spectrum of GK Vir obtained near the eclipse ($\phi \simeq 0.02$), i.e. when the heated inner hemisphere of the companion contributes least to the observed flux. By fitting the H β -H ζ Balmer lines and the He II 4686Å line they determined $T_{\text{eff}} = 48800 \pm 1200$ K and $\log g = 7.70 \pm 0.11$. They also modelled the single available far-ultraviolet spectrum of GK Vir, and obtained $T = 50000$ K. A major limitation of this spectrum obtained with *IUE* was that the photospheric Ly α line was nearly completely filled in by geocoronal emission.

We conclude that the effective temperature and distance of the white dwarf GK Vir remains somewhat uncertain, $T_{\text{eff}} \simeq 50000$ K and $d \simeq 500 \pm 50$ pc. However, it is reassuring that all the spectroscopic measurements of the surface gravity are consistent with the value that is determined from the light curve fit (see Section 4).

Fitting the He II 4686Å absorption line from the white dwarf in GK Vir gives a helium abundance of $\log[\text{He}/\text{H}] = -2.8 \pm 0.3$ by numbers. Assuming that the secondary star transfers material of solar composition, the total accretion rate is $\dot{M} \simeq 1.4 \times 10^9 \text{ g s}^{-1}$ or $2.2 \times 10^{-17} M_{\odot} \text{ yr}^{-1}$, once again consistent with other pre-CVs.

3.2.3 White dwarf radial velocity

Due to the high temperature of the white dwarf, the Balmer lines lack narrow cores and are therefore unsuitable for radial velocity work. We measured the radial velocity of the white dwarf in GK Vir from the He II 4686Å absorption line using the same technique as we used for SDSS J1212-0123. Figure 7 shows a trail of the He II line and Fig-

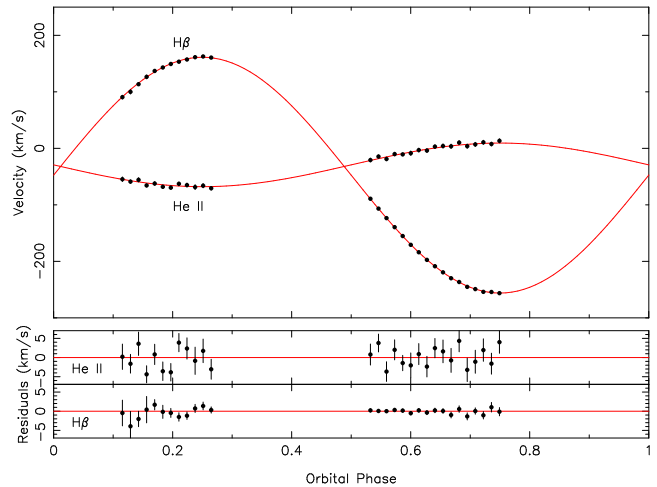


Figure 8. Radial velocity fits to the He II 4686Å absorption from the white dwarf and H β emission from the secondary star in GK Vir with residuals plotted below. The emission component does not track the centre of mass of the secondary star (see Section 3.2.5).

ure 8 shows the fitted radial velocity curve, which gives a value of $K_{\text{WD}} = 38.6 \pm 0.8 \text{ km s}^{-1}$ and a velocity offset of $\gamma_{\text{WD}} = -27.2 \pm 0.7 \text{ km s}^{-1}$.

3.2.4 Emission lines

A large number of emission lines are seen in the spectrum of GK Vir caused by the heating of the secondary star by the

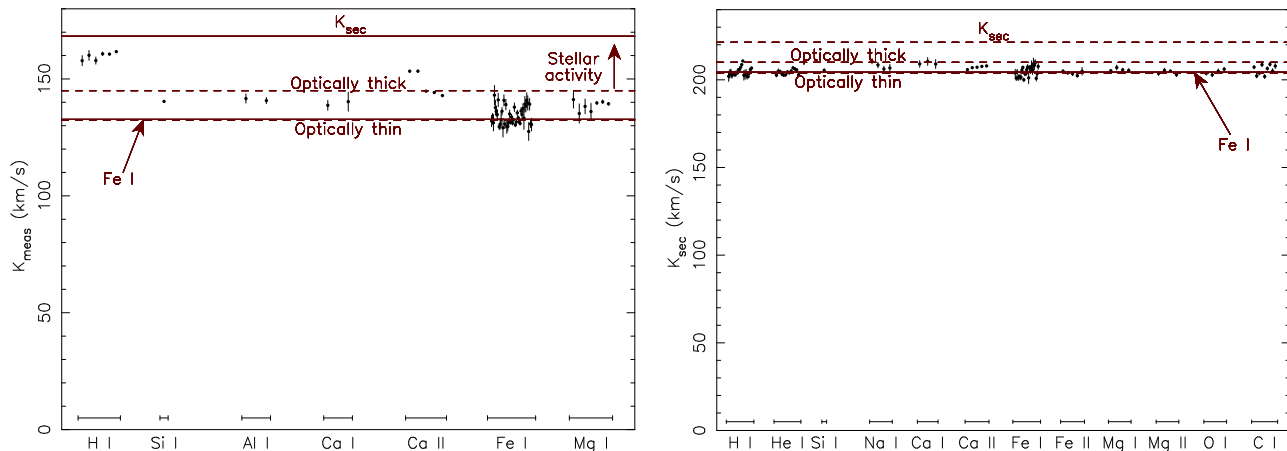


Figure 9. *Left:* radial velocities of the emission lines from the secondary star in SDSS J1212-0123. The measured value of centre of mass radial velocity (K_{sec}) is also shown. The two dashed lines denote the radial velocity that an optically thick and optically thin line would have. The solid line at 133 km s^{-1} is a weighted average of the radial velocity amplitudes of the Fe I lines, these appear to be optically thin. The radial velocity amplitudes of the hydrogen Balmer lines and the calcium H and K lines are far above the optically thick limit implying that these lines originate, at least in part, from stellar activity. *Right:* a similar plot but for GK Vir. However, in this case we were unable to directly measure K_{sec} from the spectroscopy, but by assuming that the Fe I lines are optically thin we get a consistent solution. The much tighter limits and smaller correction in GK Vir imply that the secondary star is quite small.

white dwarf. However, the secondary star in GK Vir receives a much larger irradiating flux to that in SDSS J1212-0123 due to the higher temperature of the white dwarf, therefore a larger number of lines are present and from higher ionised states. Unfortunately the strength of the Na I absorption doublet is too low after phase 0.25 and, combined with the lack of any other absorption features from the secondary star, means that we are unable to get a direct measurement of the radial velocity amplitude of the centre of mass of the secondary star. We determine the radial velocities and offsets of all of the emission lines identified using the same method used for SDSS J1212-0123, these are listed in Table A2 in the Appendix. We use these results to determine a velocity offset of $\gamma_{\text{sec}} = -47.35 \pm 0.05 \text{ km s}^{-1}$, giving a measured redshift for the white dwarf of $V_z = 20.2 \pm 0.7 \text{ km s}^{-1}$.

3.2.5 K_{sec} correction

As previously noted the emission lines in the X-shooter spectra of GK Vir cannot be used to directly measure K_{sec} , needed for accurate mass determinations. We need to determine the deviation between the reprocessed light centre and the centre of mass for the secondary star. The radial velocity of the centre of mass (K_{sec}) is related to that of the emission lines (K_{emis}) by

$$K_{\text{sec}} = \frac{K_{\text{emis}}}{1 - f(1 + q)R_{\text{sec}}/a} \quad (11)$$

(Parsons et al. 2011b), where f is a constant between 0 and 1 which depends upon the location of the centre of light. For $f = 0$ the emission is spread uniformly across the entire surface of the secondary star and therefore the centre of light is the same as the centre of mass. For $f = 1$ all of the flux is assumed to come from the point on the secondary star's surface closest to the white dwarf (the substellar point).

The centre of light for an emission line is related to the optical depth of the emission (Parsons et al. 2010a;

Parsons et al. 2011b). Optically thick emission tends to be preferentially radiated perpendicular to the stellar surface, therefore at the quadrature phases, we will see the limb of the irradiated region more prominently (compared to the region of maximum irradiation) than we would otherwise. This will lead to a higher observed semi-amplitude and hence a smaller correction factor is needed. The reverse is true for optically thin lines where the emission is radiated equally in all directions, hence emission from the substellar point becomes enhanced at quadrature, leading to a low semi-amplitude and a larger correction factor. The correction factor for an optically thin line (assuming emissivity proportional to the incident flux) is $f = 0.77$ and $f = 0.5$ for optically thick emission (Parsons et al. 2010a).

We can estimate the optical depths of the emission lines in GK Vir using our observation of SDSS J1212-0123 and assuming a similar behaviour in the lines. We can determine the optical depth of the lines in SDSS J1212-0123 because in this case we have a direct measurement of K_{sec} . Therefore, we can reverse Eq (11) to determine the optical depths. The left hand panel of Figure 9 shows where the emission lines lie with respect to the optically thin lower limit and the optically thick upper limit. We find that the measured radial velocities of the Fe I lines are consistent with them being optically thin. The majority of the emission lines in SDSS J1212-0123 appear to lie somewhere between optically thick and optically thin with the exception of the hydrogen Balmer lines and the calcium H and K lines. For these lines the measured radial velocity is far higher than the optically thick limit, implying that the emission is more uniformly spread over the surface of the secondary star, this is most likely caused by stellar activity. This is consistent with the observations of several small flares during our photometry and implies that the secondary star in SDSS J1212-0123 is an active star.

From our analysis of the emission lines in SDSS J1212-0123 we make the assumption that the Fe I lines in GK Vir

Table 7. Eclipse times for GK Vir. (1) Green et al. (1978), (2) Parsons et al. (2010b), (3) this paper.

Cycle No.	MJD(BTDB) (mid-eclipse)	Reference
-67	42520.26747(1)	(1)
-32	42532.31905(2)	(1)
-29	42533.35204(9)	(1)
0	42543.33769(1)	(1)
3	42544.37068(1)	(1)
851	42836.36314(6)	(1)
1966	43220.29202(12)	(1)
2132	43277.45101(6)	(1)
2896	43540.51972(12)	(1)
28666	52413.9255716(9)	(2)
29735	52782.0152272(9)	(2)
29738	52783.0482185(7)	(2)
30746	53130.1336878(27)	(2)
32706	53805.0221154(23)	(2)
32709	53806.0551129(12)	(2)
34054	54269.1800868(3)	(2)
37069	55307.3375852(11)	(3)

are also optically thin. We can then use their radial velocities to predict K_{sec} using Eq (11). We adopt a value for the radial velocity amplitude of an optically thin line of $K_{\text{Thin}} = 204 \pm 2 \text{ km s}^{-1}$. We use this result as a prior constraint in our light curve fitting. The right hand panel of Figure 9 shows the radial velocity amplitudes of the emission lines in GK Vir, the dashed lines are based on the results of our light curve fitting (see section 3.2.8). The spread in the emission line radial velocities in GK Vir is relatively small compared to SDSS J1212-0123 because of the small relative size of the secondary star (R_{sec}/a).

3.2.6 Eclipse times

We recorded one new high precision eclipse time for GK Vir which is listed in Table 7 along with all previous eclipse times. We update the ephemeris to

$$\begin{aligned} \text{MJD(BTDB)} &= 42543.337\,9121(33) \\ &+ 0.344\,330\,832\,742(99)E, \end{aligned}$$

which is consistent with previous studies. Figure 10 shows the difference between the observed eclipse time and the calculated eclipse time based on our new ephemeris. Our new eclipse time shows a clear deviation from linearity, although the magnitude of the period change is small compared to other systems (see Parsons et al. 2010b). The secondary star in GK Vir is able to drive this small period change (0.00124 seconds in ~ 8 years) via Applegate’s mechanism (Applegate 1992), although this is only just the case if we used the modified version of Applegate’s mechanism presented by Brinkworth et al. (2006) which takes account of the role of the inner part of the star in counterbalancing the outer shell. A third body in orbit around the system may also be the cause of the period change, as has recently been proposed for NN Ser (Beuermann et al. 2010), however, longer term monitoring is required in order to discover the true cause of this period change.

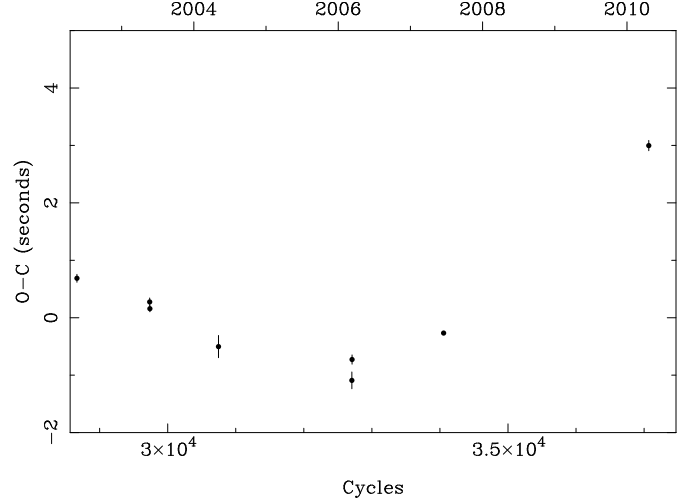


Figure 10. Observed-Calculated (O-C) plot for the eclipse times of GK Vir. Our new point shows a departure from linearity in the eclipse times. The secondary star is just able to supply the energy required to drive this period change via Applegate’s mechanism however, a third body in orbit around the system is also a possible explanation.

3.2.7 Spectral type of the secondary star

We detect the secondary star in GK Vir in the r' , i' and J band eclipses. We measure magnitudes of $r' = 21.72 \pm 0.03$, $i' = 19.98 \pm 0.01$ and $J = 17.59 \pm 0.05$. The $r' - i' = 1.74 \pm 0.03$ colour is consistent with a spectral type of M4.5 whilst the $i' - J = 2.39 \pm 0.05$ is closer to a spectral type of M4 (Hawley et al. 2002). Using the distance from our spectroscopic fit ($550 \pm 20 \text{ pc}$) the secondary star has an absolute J band magnitude of $M_J = 8.9$, giving it a spectral type of M4.5 (Hawley et al. 2002), therefore we adopt a spectral type of $M4.5 \pm 0.5$.

3.2.8 Modelling the light curves

The light curves of GK Vir show a deep eclipse of the white dwarf even in the J band. GK Vir shows a small reflection effect out of eclipse, however no secondary eclipse is detected. We fit the light curves of GK Vir in the same way as those of SDSS J1212-0123 (see Section 3.1.8). However, since we lack a direct measurement of K_{sec} , we use our constraint on K_{Thin} and Eq (11) as well as our K_{WD} and gravitational redshift measurements to constrain the inclination.

We phase binned the data, using smaller bins on the ingress and egress, and kept the period fixed as one when fitting the light curves. We also kept the temperature of the white dwarf fixed at 55,995K. For the secondary star we used quadratic limb darkening coefficients from Claret & Bloemen (2011) for a $T_{\text{eff}} = 3000 \text{ K}$, $\log g = 5$ main sequence star. For the white dwarf we calculated quadratic limb darkening coefficients from a white dwarf model with $T_{\text{WD}} = 55,995$ and $\log g = 7.68$ based on our spectroscopic fits, folded through the ULTRACAM u' , g' , r' and i' and SOFI J filter profiles. For both stars we quote the coefficients a and b where $I(\mu)/I(1) = 1 - a(1 - \mu) - b(1 - \mu)^2$, where μ is the cosine of the angle between the line of sight and the surface normal, we kept all limb darkening parameters

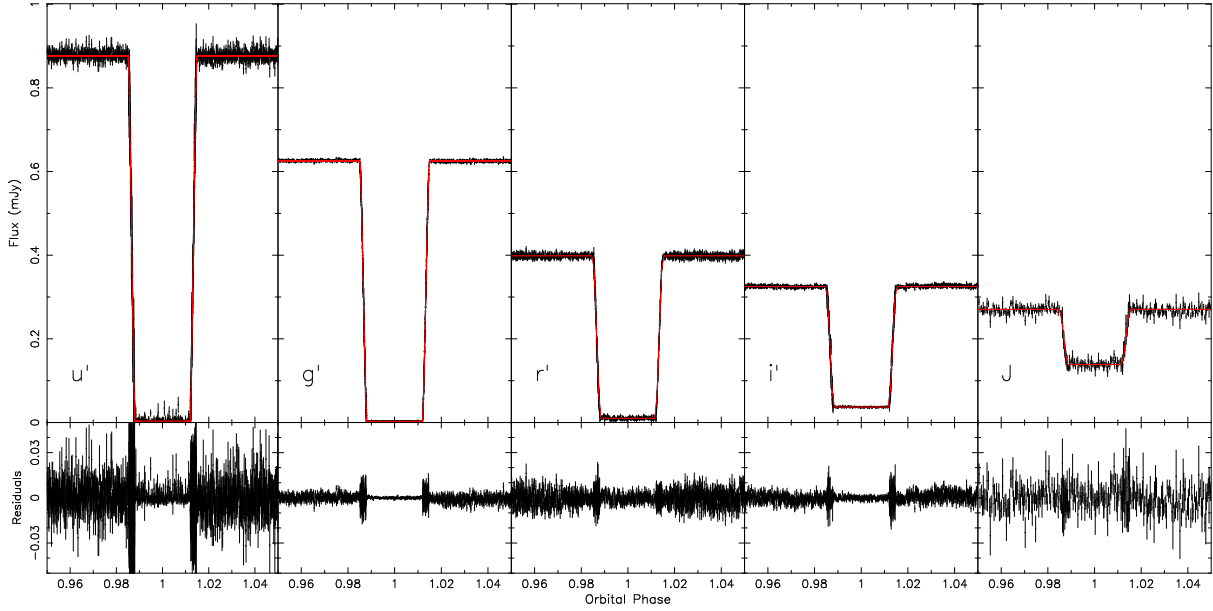


Figure 11. ULTRACAM u' , g' , r' and i' and SOFI J band primary eclipses of GK Vir with model fits and residuals. The light curves have been binned up by a factor of 5 although smaller bins were used on the ingress and egress features, which leads to the small spikes seen in the residuals at the ingress and egress.

Table 8. Parameters from Markov chain Monte Carlo minimisation for GK Vir, some fitted, some fixed a priori (those without quoted uncertainties). a and b are the quadratic limb darkening coefficients. A is the fraction of the irradiating flux from the white dwarf absorbed by the secondary star, this was kept fixed for the r' band since there is little coverage out-of-eclipse in this band.

Parameter	u'	g'	r'	i'	J
i (deg)	89.5 ± 0.7	89.5 ± 0.6	89.3 ± 0.9	89.2 ± 0.9	88.8 ± 1.4
r_{WD}/a	0.0093 ± 0.0002	0.0094 ± 0.0002	0.0093 ± 0.0003	0.0094 ± 0.0003	0.0097 ± 0.0006
r_{sec}/a	0.085 ± 0.002	0.085 ± 0.002	0.086 ± 0.002	0.086 ± 0.003	0.088 ± 0.006
$T_{\text{eff,sec}}$ (K)	3113 ± 31	3270 ± 12	3224 ± 28	3508 ± 40	4117 ± 139
a_{WD}	0.0769	0.0594	0.0505	0.0446	0.0257
b_{WD}	0.1393	0.1165	0.0896	0.0736	0.0490
a_{sec}	0.5866	0.6720	0.6364	0.4193	0.0254
b_{sec}	0.2959	0.2660	0.2521	0.4109	0.4826
A	1.055 ± 0.039	0.551 ± 0.006	0.400	0.263 ± 0.009	0.245 ± 0.032
K_{sec}	221.0 ± 2.1	221.2 ± 2.1	221.1 ± 2.1	221.3 ± 2.1	222.5 ± 2.3

fixed. For our r' band light curve we lack any out of eclipse information (barring that immediately before and after the eclipse) hence A , the fraction of irradiating flux absorbed by the secondary star, is unconstrained. Therefore, we fix this value at 0.4; this parameter has no effect on the radii or inclination.

Figure 11 shows the fits to the light curves and the residuals and our final fitted parameters are listed in Table 8. We also list the limb darkening coefficients used for each band.

4 DISCUSSION

Our light curve fits combined with Eqs (5)-(8) yield direct measurements for the masses and radii of both components in SDSS J1212-0123 and GK Vir. For our final values and uncertainties we combine the results of all our light curves,

however, since they are all constrained by the same spectroscopic information the uncertainties in each light curve fit are not independent. Therefore we combine the results from each light curve in an optimal way by calculating the minimum possible error on each parameter purely from the spectroscopic constraints and then combining parameters allowing for the correlated and random noise components. Our final parameters for both systems are listed in Table 9. The secondary star's shape in both systems is slightly distorted due to the presence of the nearby white dwarf, therefore Table 9 lists the radius of the secondary star in various directions. This is a very minor effect in GK Vir whilst the effect is somewhat larger for SDSS J1212-0123, though in both cases the variations are smaller than the uncertainty on the radius from the light curve fits. For our final discussions we adopt the volume-averaged radii.

Figure 12 shows the mass-radius plot for white dwarfs. The position of the white dwarfs in SDSS J1212-0123 and

Table 9. System parameters. The surface gravities quoted are from the spectroscopic fit. They are consistent with the measured masses and radii. The accretion rate is that of the material from the wind of the secondary star onto the white dwarf

Parameter	SDSS J1212-0123	GK Vir
Period (days)	0.335 871 14(13)	0.344 330 832 742(99)
Inclination	$85.7^\circ \pm 0.5^\circ$	$89.5^\circ \pm 0.6^\circ$
Binary separation	$1.815 \pm 0.003 R_\odot$	$1.82 \pm 0.01 R_\odot$
Mass ratio	0.620 ± 0.001	0.174 ± 0.004
WD mass	$0.439 \pm 0.002 M_\odot$	$0.564 \pm 0.014 M_\odot$
Sec mass	$0.273 \pm 0.002 M_\odot$	$0.116 \pm 0.003 M_\odot$
WD radius	$0.0168 \pm 0.0003 R_\odot$	$0.0170 \pm 0.0004 R_\odot$
Sec radius polar	$0.304 \pm 0.007 R_\odot$	$0.154 \pm 0.003 R_\odot$
Sec radius sub-stellar	$0.310 \pm 0.007 R_\odot$	$0.156 \pm 0.003 R_\odot$
Sec radius backside	$0.309 \pm 0.007 R_\odot$	$0.156 \pm 0.003 R_\odot$
Sec radius side	$0.306 \pm 0.007 R_\odot$	$0.155 \pm 0.003 R_\odot$
Sec radius volume-averaged	$0.306 \pm 0.007 R_\odot$	$0.155 \pm 0.003 R_\odot$
WD log g	7.51 ± 0.01	7.68 ± 0.04
WD temperature	$17,707 \pm 35\text{K}$	$55,995 \pm 673\text{K}$
K_{WD}	$104.4 \pm 0.5 \text{ km s}^{-1}$	$38.6 \pm 0.8 \text{ km s}^{-1}$
K_{sec}	$168.3 \pm 0.3 \text{ km s}^{-1}$	$221.6 \pm 2.0 \text{ km s}^{-1}$
$V_{z,\text{WD}}$	$16.1 \pm 0.3 \text{ km s}^{-1}$	$20.2 \pm 0.7 \text{ km s}^{-1}$
Sec spectral type	M4	M4.5 \pm 0.5
Distance	$228 \pm 5 \text{ pc}$	$550 \pm 20 \text{ pc}$
Accretion rate	$6.4 \times 10^{-17} M_\odot \text{ yr}^{-1}$	$2.2 \times 10^{-17} M_\odot \text{ yr}^{-1}$

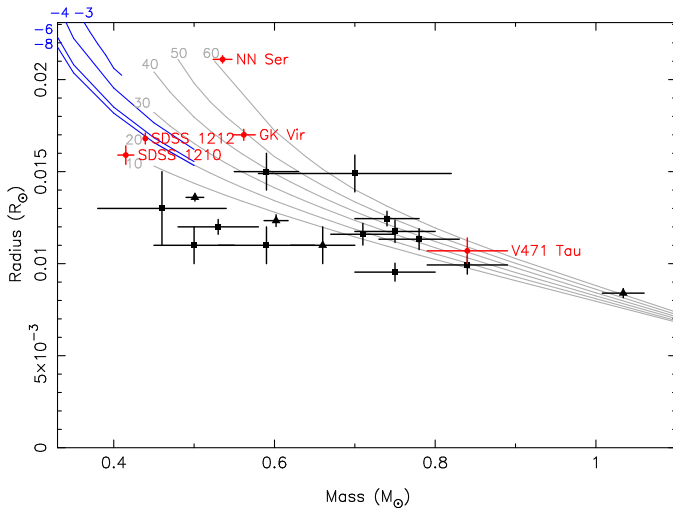


Figure 12. Mass-radius plot for white dwarfs. Black points are from Provencal et al. (1998), Provencal et al. (2002) and Casewell et al. (2009). The square points are common proper-motion systems, the triangular points are visual binaries. White dwarfs measurements from PCEBs are shown in red (online version only) from (O’Brien et al. 2001), Parsons et al. (2010a), Pyrzas et al. (2011) and this work. The grey lines are CO core models with the temperatures labelled in units of 10^3K and with hydrogen layer thicknesses of $M_{\text{H}}/M_{\text{WD}} = 10^{-4}$ from Benvenuto & Althaus (1999). The mass and radius of the white dwarf in GK Vir agree well with the 50,000K model. The blue lines (online version only) are He core models with a temperature of 18,000K and varying hydrogen layer thicknesses labelled by the exponent of the hydrogen layer fraction, from Panei et al. (2007). The mass and radius of the white dwarf in SDSS J1212-0123 is consistent with the CO core models for its temperature but we can rule out a CO core on evolutionary grounds. Therefore the white dwarf in SDSS J1212-0123 is consistent with the He core models only if it has a very thin hydrogen envelope ($M_{\text{H}}/M_{\text{WD}} \leq 10^{-6}$).

GK Vir are shown as well as other accurate white dwarf mass-radius measurements. The measured mass and radius of the white dwarf in GK Vir are consistent with a carbon-oxygen (CO) core white dwarf of the same temperature, with a thick hydrogen envelope ($M_{\text{H}}/M_{\text{WD}} = 10^{-4}$). The measured mass and radius of the white dwarf in SDSS J1212-0123 are also consistent with a CO core white dwarf with the same temperature and a thick hydrogen envelope ($M_{\text{H}}/M_{\text{WD}} = 10^{-4}$). However, although it is possible to create CO core white dwarfs with masses $< 0.5 M_\odot$ via considerable mass loss along the red giant phase (Prada Moroni & Straniero 2009; Willems & Kolb 2004; Han et al. 2000), doing so in a binary system requires a large initial mass ratio and results in a widening of the orbital separation, hence we would not expect a CO core white dwarf with a mass $< 0.5 M_\odot$ in a close binary system. Therefore the white dwarf in SDSS J1212-0123 must have a He core, as noted by Shen et al. (2009).

Several He core mass-radius relations are shown in Figure 12 for a white dwarf with a temperature of 18,000K and varying hydrogen layer thicknesses. The white dwarf in SDSS J1212-0123 is consistent with these relations only if it has a very thin hydrogen envelope ($M_{\text{H}}/M_{\text{WD}} \leq 10^{-6}$). Figure 13 shows a zoomed in version of the mass radius plot for the white dwarf in SDSS J1212-0123 as well as the same He core models as Figure 12. The black line shows the range of possible masses and radii that the white dwarf in SDSS J1212-0123 could have based on the radial velocities and the primary eclipse shape (i.e. no inclination constraints). The numbers plotted along this line are what the measured gravitational redshift of the white dwarf would need to be in order to give that mass and radius. Previous studies have found that the spectroscopic gravitational redshift measurements are usually slightly inconsistent with mass-radius measurements via other methods (Pyrzas et al. 2011; Parsons et al. 2010a; Maxted et al. 2007) meaning that our inclination constraints may be slightly incorrect.

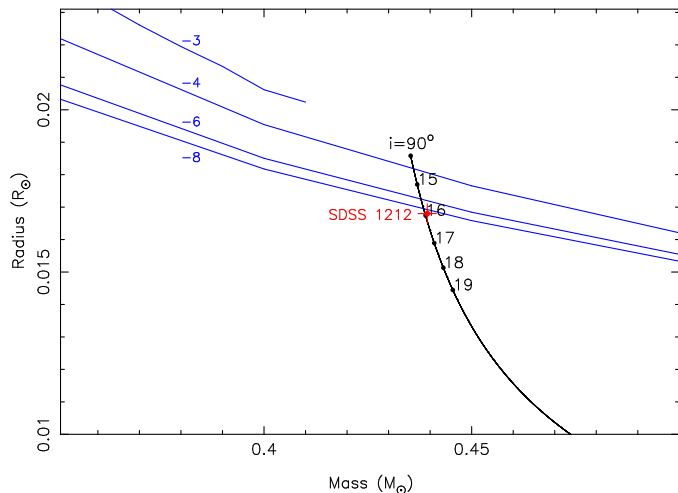


Figure 13. Mass-radius plot for the white dwarf in SDSS J1212-0123. The blue lines (online version only) are He core models with a temperature of 18,000K and varying hydrogen layer thicknesses labelled by the exponent of the hydrogen layer fraction, from Panei et al. (2007). The black line shows the possible mass and radius range without any constraint on the inclination with 90° at the top. The numbers along this line correspond to the gravitational redshift that the white dwarf would have at that inclination (in km s^{-1}). Our measured redshift ($16.1 \pm 0.3 \text{ km s}^{-1}$) means that the white dwarf is consistent with models which have a thin hydrogen layer. However, even without any inclination constraints it is not possible for the white dwarf to have a thick ($M_{\text{H}}/M_{\text{WD}} > 2 \times 10^{-4}$) hydrogen layer.

However, Figure 13 shows that it is not possible for the white dwarf to have a thick hydrogen envelope ($M_{\text{H}}/M_{\text{WD}} > 2 \times 10^{-4}$) even if the inclination is 90° . Current evolutionary models are unable to create He core white dwarfs with such thin hydrogen envelopes, the thinnest envelopes are of the order of $M_{\text{H}}/M_{\text{WD}} \sim 3 \times 10^{-4}$ (Althaus et al. 2009; Sarna et al. 2000; Driebe et al. 1998) meaning that, assuming our measured V_z value is accurate, either SDSS J1212-0123 has had a very unusual evolutionary history or that current evolutionary models of He core white dwarfs are incomplete and overestimate their size. Additional He core white dwarf mass-radius measurements should show if this is the case.

Figure 14 show the mass-radius plot for low mass stars. The masses and radii of the secondary stars in SDSS J1212-0123 and GK Vir are marked as well as other precise measurements. The mass and radius of the secondary star in SDSS J1212-0123 show that it is over-inflated for its mass compared with evolutionary models by ~ 12 per cent. This discrepancy can be reduced to ~ 9 per cent if the secondary star is active. In this case the radius may be overestimated due to the effects of polar spots, it also increases to compensate for loss of radiative efficiency due to starspots and due to a strong magnetic field caused by rapid rotation (Morales et al. 2010; Chabrier et al. 2007). We have evidence from the emission lines and light curves that the secondary star in SDSS J1212-0123 is indeed active, therefore

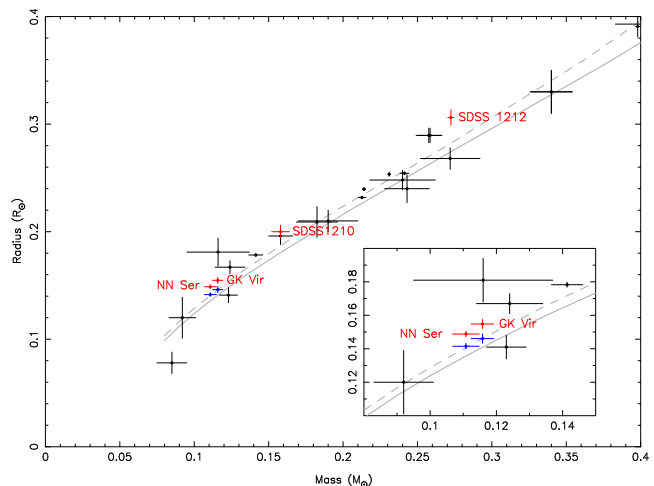


Figure 14. Mass-radius plot for low-mass stars. Black points are high-precision measurements taken from Knigge et al. (2011), Carter et al. (2011) and Ofir et al. (2011). The solid line is the 4.0-Gyr isochrone from Baraffe et al. (1998) whilst the dashed line is a 4.0-Gyr model from Morales et al. (2010) which includes the effects of magnetic activity. Low-mass stars from PCEBs are shown in red (online version only) from Parsons et al. (2010a), Pyrzas et al. (2011) and this work. The blue points (online version only) show the radii of these stars after correcting for irradiation (negligible for SDSS J1210+3347 and SDSS J1212-0123). The secondary star in GK Vir is consistent with model predictions after correcting for irradiation, however the secondary star in SDSS J1212-0123 is still oversized.

these effects can explain some of the discrepancy however, the star remains oversized. The secondary star in GK Vir is also oversized by ~ 9 per cent, this drops to ~ 6 per cent if it is active, though we have no evidence of activity from this star.

Taking the effects of rotational and tidal perturbations fully into account only causes an increase in the radii of 0.1 per cent for GK Vir and 0.4 per cent for SDSS J1212-0123 (Sirotkin & Kim 2009) which is not enough to explain the discrepancy.

Irradiation by the white dwarf can cause the secondary star to become inflated by effectively blocking the energy outflow through the surface layers (Ritter et al. 2000). For NN Ser correcting this effect brought the mass and radius measurements into agreement with evolutionary models (Parsons et al. 2010a). For the secondary star in GK Vir we find that irradiation increases its radius by 5.6% (Ritter et al. 2000; Hameury & Ritter 1997), enough to bring it into agreement with evolutionary models. However, for the far less irradiated secondary star in SDSS J1212-0123 we find an increase of only 0.4% meaning that it is still overinflated. The corrected radii are shown in Figure 14

5 CONCLUSIONS

We have used a combination of ULTRACAM and SOFI photometry and X-shooter spectroscopy to measure precise masses and radii for both components of the eclipsing PCEBs SDSS J1212-0123 and GK Vir. In both cases we use measurements of the gravitational redshift of the white

dwarf to constrain the orbital inclination. We were able to directly measure the radial velocity amplitudes of both stars in SDSS J1212-0123 but only the white dwarf in GK Vir. However, we use our results from SDSS J1212-0123 and information from the emission lines to determine the correction factor to apply to the emission line radial velocities in GK Vir to measure the centre of mass radial velocity of the secondary star. The mass and radius of the $0.564 M_{\odot}$ white dwarf in GK Vir are consistent with evolutionary models for a CO core white dwarf with a thick hydrogen envelope. The mass and radius of the white dwarf in SDSS J1212-0123 place it in the crossover region between a CO core white dwarf and a He core white dwarf but we can exclude a CO core on evolutionary grounds. This means that the white dwarf in SDSS J1212-0123 is the first He core white dwarf with precise mass-radius measurements however, it is under-inflated for its temperature unless it has a very thin ($M_{\text{H}}/M_{\text{WD}} \leq 10^{-6}$) hydrogen envelope, which evolutionary models are unable to produce. The mass and radius of the secondary star in GK Vir are consistent with evolutionary models after correcting for the effects of irradiation by the white dwarf, however, the secondary star in SDSS J1212-0123 is overinflated compared to theoretical predictions even after the effects of activity, rapid rotation and irradiation are taken into account.

ACKNOWLEDGEMENTS

We thank the anonymous referee for their useful comments and suggestions. ULTRACAM, TRM, BTG, CMC, VSD and SPL are supported by the Science and Technology Facilities Council (STFC). SPL also acknowledges the support of an RCUK Fellowship. ARM acknowledges financial support from FONDECYT in the form of grant number 3110049. MRS thanks for support from FONDECYT (1100782). The results presented in this paper are based on observations collected at the European Southern Observatory under programme IDs 085.D-0541 and 087.D-0046. We used the National Institute of Standards and Technology (NIST) Atomic Spectra Database (version 4.0.1).

REFERENCES

- Althaus L. G., Panei J. A., Romero A. D., Rohrmann R. D., Córscico A. H., García-Berro E., Miller Bertolami M. M., 2009, *A&A*, 502, 207
- Andersen J., 1991, *A&A Rev.*, 3, 91
- Applegate J. H., 1992, *ApJ*, 385, 621
- Baraffe I., Chabrier G., Allard F., Hauschildt P. H., 1998, *A&A*, 337, 403
- Barstow M. A., Bond H. E., Holberg J. B., Burleigh M. R., Hubeny I., Koester D., 2005, *MNRAS*, 362, 1134
- Bayless A. J., Orosz J. A., 2006, *ApJ*, 651, 1155
- Benvenuto O. G., Althaus L. G., 1999, *MNRAS*, 303, 30
- Berger D. H., Gies D. R., McAlister H. A., ten Brummelaar T. A., Henry T. J., Sturmman J., Sturmman L., Turner N. H., Ridgway S. T., Aufdenberg J. P., Mérand A., 2006, *ApJ*, 644, 475
- Beuermann K., Hessman F. V., Dreizler S., Marsh T. R., Parsons S. G., Winget D. E., Miller G. F., Schreiber M. R., Kley W., Dhillon V. S., Littlefair S. P., Copperwheat C. M., Hermes J. J., 2010, *A&A*, 521, L60+
- Brinkworth C. S., Marsh T. R., Dhillon V. S., Knigge C., 2006, *MNRAS*, 365, 287
- Brown W. R., Kilic M., Hermes J. J., Allende Prieto C., Kenyon S. J., Winget D. E., 2011, *ApJ*, 737, L23+
- Carter J. A. et al., 2011, *Science*, 331, 562
- Casewell S. L., Dobbie P. D., Napiwotzki R., Burleigh M. R., Barstow M. A., Jameson R. F., 2009, *MNRAS*, 395, 1795
- Chabrier G., Gallardo J., Baraffe I., 2007, *A&A*, 472, L17
- Claret A., Bloemen S., 2011, *A&A*, 529, A75+
- Copperwheat C. M., Marsh T. R., Dhillon V. S., Littlefair S. P., Hickman R., Gänsicke B. T., Southworth J., 2010, *MNRAS*, 402, 1824
- Debes J. H., 2006, *ApJ*, 652, 636
- Dhillon V. S., Marsh T. R., Stevenson M. J., Atkinson D. C., Kerry P., Peacocke P. T., Vick A. J. A., Beard S. M., Ives D. J., Lunney D. W., McLay S. A., Tierney C. J., Kelly J., Littlefair S. P., Nicholson R., Pashley R., Harlaftis E. T., O'Brien K., 2007, *MNRAS*, 378, 825
- D'Odorico S., Dekker H., Mazzoleni R., Vernet J., Guinouard I., Groot P., Hammer F., Rasmussen P. K., Kaper L., Navarro R., Pallavicini R., Peroux C., Zerbi F. M., 2006, in *Proc. SPIE Vol. 6269*. p. 98
- Driebe T., Schoenberner D., Bloeker T., Herwig F., 1998, *A&A*, 339, 123
- Fulbright M. S., Liebert J., Bergeron P., Green R., 1993, *ApJ*, 406, 240
- Green R. F., Richstone D. O., Schmidt M., 1978, *ApJ*, 224, 892
- Green R. F., Schmidt M., Liebert J., 1986, *ApJS*, 61, 305
- Hameury J.-M., Ritter H., 1997, *A&AS*, 123, 273
- Hamuy M., Walker A. R., Suntzeff N. B., Gigoux P., Heathcote S. R., Phillips M. M., 1992, *PASP*, 104, 533
- Han Z., Tout C. A., Eggleton P. P., 2000, *MNRAS*, 319, 215
- Hawley S. L. et al., 2002, *AJ*, 123, 3409
- Knigge C., Baraffe I., Patterson J., 2011, *ApJS*, 194, 28
- Koester D., 2010, *Mem. Soc. Astron. Italiana*, 81, 921
- Koester D., Wilken D., 2006, *A&A*, 453, 1051
- Kraus A. L., Tucker R. A., Thompson M. I., Craine E. R., Hillenbrand L. A., 2011, *ApJ*, 728, 48
- Liebert J., Bergeron P., Holberg J. B., 2005, *ApJS*, 156, 47
- Littlefair S. P., Dhillon V. S., Marsh T. R., Gänsicke B. T., Southworth J., Baraffe I., Watson C. A., Copperwheat C., 2008, *MNRAS*, 388, 1582
- López-Morales M., 2007, *ApJ*, 660, 732
- Maxted P. F. L., O'Donoghue D., Morales-Rueda L., Napiwotzki R., Smalley B., 2007, *MNRAS*, 376, 919
- Moorwood A., Cuby J.-G., Lidman C., 1998, *The Messenger*, 91, 9
- Morales J. C., Gallardo J., Ribas I., Jordi C., Baraffe I., Chabrier G., 2010, *ApJ*, 718, 502
- Morales J. C., Ribas I., Jordi C., 2008, *A&A*, 478, 507
- Nebot Gómez-Morán A., Schwöpe A. D., Schreiber M. R., Gänsicke B. T., Pyrzas S., Schwarz R., Southworth J., Kohnert J., Vogel J., Krumpke M., Rodríguez-Gil P., 2009, *A&A*, 495, 561
- O'Brien M. S., Bond H. E., Sion E. M., 2001, *ApJ*, 563, 971

- Ofir A., Gandolfi D., Buchhave L., Lacy C. H. S., Hatzes A. P., Fridlund M., 2011, ArXiv e-prints
- Panei J. A., Althaus L. G., Chen X., Han Z., 2007, MNRAS, 382, 779
- Parsons S. G., Marsh T. R., Copperwheat C. M., Dhillon V. S., Littlefair S. P., Gänsicke B. T., Hickman R., 2010a, MNRAS, 402, 2591
- Parsons S. G., Marsh T. R., Copperwheat C. M., Dhillon V. S., Littlefair S. P., Hickman R. D. G., Maxted P. F. L., Gänsicke B. T., Unda-Sanzana E., Colque J. P., Barraza N., Sánchez N., Monard L. A. G., 2010b, MNRAS, 407, 2362
- Parsons S. G., Marsh T. R., Gänsicke B. T., Drake A. J., Koester D., 2011a, ApJ, 735, L30+
- Parsons S. G., Marsh T. R., Gänsicke B. T., Dhillon V. S., Copperwheat C. M., Littlefair S. P., Pyrzas S., Drake A. J., Koester D., Schreiber M. R., Rebassa-Mansergas A., 2011b, ArXiv e-prints
- Prada Moroni P. G., Straniero O., 2009, A&A, 507, 1575
- Press W. H., Teukolsky A. A., Vetterling W. T., Flannery B. P., 2007, Numerical recipes. The art of scientific computing, 3rd edn.. Cambridge: University Press
- Provencal J. L., Shipman H. L., Hog E., Thejll P., 1998, ApJ, 494, 759
- Provencal J. L., Shipman H. L., Koester D., Wesemael F., Bergeron P., 2002, ApJ, 568, 324
- Pyrzas S., Gänsicke B. T., Brady S., Parsons S. G., Marsh T. R., Koester D., Breedt E., Copperwheat C. M., Nebot Gomez-Moran A., Rebassa-Mansergas A., Schreiber M. R., Zorotovic M., 2011, ArXiv e-prints
- Pyrzas S., Gänsicke B. T., Marsh T. R., Aungwerojwit A., Rebassa-Mansergas A., Rodríguez-Gil P., Southworth J., Schreiber M. R., Nebot Gomez-Moran A., Koester D., 2009, MNRAS, 394, 978
- Rebassa-Mansergas A., Gänsicke B. T., Rodríguez-Gil P., Schreiber M. R., Koester D., 2007, MNRAS, 382, 1377
- Rebassa-Mansergas A., Gänsicke B. T., Schreiber M. R., Koester D., Rodríguez-Gil P., 2010, MNRAS, 402, 620
- Renzini A., Bragaglia A., Ferraro F. R., Gilmozzi R., Ortolani S., Holberg J. B., Liebert J., Wesemael F., Bohlin R. C., 1996, ApJ, 465, L23+
- Ribas I., 2006, Ap&SS, 304, 89
- Richards G. T. et. al., 2004, ApJS, 155, 257
- Ritter H., Zhang Z.-Y., Kolb U., 2000, A&A, 360, 969
- Sarna M. J., Ergma E., Gerškevičš-Antipova J., 2000, MNRAS, 316, 84
- Savory C. D. J., Littlefair S. P., Dhillon V. S., Marsh T. R., Gänsicke B. T., Copperwheat C. M., Kerry P., Hickman R. D. G., Parsons S. G., 2011, MNRAS, 415, 2025
- Shen K. J., Idan I., Bildsten L., 2009, ApJ, 705, 693
- Silvestri N. M. et. al., 2006, AJ, 131, 1674
- Sirotkin F. V., Kim W.-T., 2009, ApJ, 698, 715
- Skrutskie M. F. et al., 2006, AJ, 131, 1163
- Smith J. A. et al., 2002, AJ, 123, 2121
- Southworth J., Bruntt H., Buzasi D. L., 2007, A&A, 467, 1215
- Southworth J., Smalley B., Maxted P. F. L., Claret A., Etzel P. B., 2005, MNRAS, 363, 529
- Steinfadt J. D. R., Kaplan D. L., Shporer A., Bildsten L., Howell S. B., 2010, ApJ, 716, L146
- Tappert C., Gänsicke B. T., Rebassa-Mansergas A., Schmidtbreick L., Schreiber M. R., 2011, A&A, 531, A113+
- Torres G., 2007, ApJ, 671, L65
- Torres G., Andersen J., Giménez A., 2010, A&A Rev., 18, 67
- Vennes S., Kawka A., Németh P., 2011a, MNRAS, 413, 2545
- Vennes S. et al., 2011b, ApJ, 737, L16+
- Willems B., Kolb U., 2004, A&A, 419, 1057
- Wood M. A., 1992, ApJ, 386, 539

APPENDIX A: EMISSION LINES

Table A1. Secondary star emission lines in SDSS J1212-0123. After measuring the radial velocity of a line, the spectra were shifted to remove the motion and averaged. The Equivalent widths were measured from this averaged spectrum.

Line	γ_{sec} (km/s)	K_{meas} (km/s)	Equivalent Width (mÅ)
Mg I 3829.355	18.31 ± 2.52	141.19 ± 3.68	72 ± 3
Mg I 3832.299	22.90 ± 3.20	135.22 ± 4.12	60 ± 3
Mg I 3838.292	17.09 ± 2.25	138.27 ± 3.17	67 ± 3
Fe I 3878.573	18.74 ± 1.89	132.01 ± 2.41	83 ± 2
H8 3889.055	17.47 ± 1.73	157.82 ± 2.18	74 ± 3
Si I 3905.523	22.79 ± 0.33	140.42 ± 0.43	248 ± 2
Fe I 3922.911	20.92 ± 1.86	132.93 ± 2.32	41 ± 2
Fe I 3928.083	15.52 ± 2.49	131.28 ± 3.52	37 ± 2
Ca II 3933.663	22.31 ± 0.38	153.32 ± 0.48	386 ± 3
Al I 3944.006	25.21 ± 1.41	141.63 ± 1.99	48 ± 2
Al I 3961.520	19.95 ± 1.01	140.74 ± 1.35	72 ± 2
Ca II 3968.469	21.05 ± 0.53	153.32 ± 0.48	349 ± 3
Hε 3970.074	17.03 ± 2.88	160.10 ± 2.13	84 ± 2
Hδ 4101.735	21.62 ± 1.23	157.86 ± 1.53	262 ± 4
Fe I 4143.868	22.17 ± 2.91	143.06 ± 4.15	31 ± 2
Fe I 4216.184	20.09 ± 2.30	137.76 ± 3.16	27 ± 2
Ca I 4226.728	22.94 ± 1.59	138.71 ± 2.13	91 ± 2
Hγ 4340.465	17.31 ± 0.60	160.76 ± 0.76	320 ± 3
Fe I 4375.986	21.88 ± 1.73	136.22 ± 2.20	54 ± 2
Fe I 4427.310	19.64 ± 1.57	134.77 ± 2.09	49 ± 2
Fe I 4461.653	20.38 ± 2.23	141.02 ± 2.91	47 ± 2
Fe I 4482.170	20.86 ± 1.09	129.57 ± 1.22	36 ± 2
Mg I 4571.096	16.38 ± 2.98	136.07 ± 3.55	23 ± 2
Hβ 4861.327	19.97 ± 0.32	160.61 ± 0.40	675 ± 4
Fe I 4924.298	19.42 ± 1.46	130.66 ± 2.18	65 ± 2
Fe I 4939.686	18.22 ± 2.34	132.61 ± 3.18	29 ± 2
Fe I 4957.597	19.55 ± 1.07	136.19 ± 1.63	48 ± 1
Fe I 5006.119	21.48 ± 2.64	129.10 ± 3.95	32 ± 2
Fe I 5012.068	15.55 ± 1.77	140.84 ± 2.42	46 ± 2
Fe I 5041.447	20.98 ± 1.45	130.69 ± 1.91	91 ± 2
Fe I 5051.664	18.19 ± 1.64	139.04 ± 2.28	41 ± 2
Fe I 5079.740	23.25 ± 2.15	129.63 ± 2.89	48 ± 2
Fe I 5083.338	19.40 ± 1.56	129.62 ± 2.01	30 ± 2
Fe I 5107.447	19.03 ± 1.19	131.36 ± 1.63	82 ± 2
Fe I 5110.413	17.30 ± 1.29	135.01 ± 1.71	87 ± 2
Mg I 5167.322	17.26 ± 0.45	139.73 ± 0.59	150 ± 2
Fe I 5168.898	19.56 ± 0.75	131.56 ± 0.96	78 ± 2
Mg I 5172.684	20.00 ± 0.56	140.22 ± 0.78	254 ± 3
Mg I 5183.604	17.46 ± 0.46	139.37 ± 0.62	209 ± 2
Fe I 5227.189	21.54 ± 0.85	133.72 ± 1.16	76 ± 2
Fe I 5269.537	22.13 ± 0.61	131.14 ± 0.85	173 ± 2
Fe I 5328.038	21.83 ± 0.42	132.58 ± 0.58	160 ± 2
Fe I 5341.234	22.18 ± 1.35	137.92 ± 1.86	83 ± 2
Fe I 5371.489	15.66 ± 0.60	130.31 ± 0.82	101 ± 2
Fe I 5397.128	17.84 ± 0.63	131.63 ± 0.87	103 ± 2
Fe I 5405.774	20.25 ± 0.85	135.49 ± 1.16	75 ± 2
Fe I 5429.695	20.10 ± 0.60	133.37 ± 0.84	97 ± 2
Fe I 5446.871	19.61 ± 0.56	131.62 ± 0.74	152 ± 2
Fe I 5455.609	20.32 ± 0.56	130.99 ± 0.76	121 ± 2
Fe I 5497.516	21.74 ± 1.09	136.31 ± 1.49	85 ± 2
Fe I 5501.465	18.64 ± 1.78	134.74 ± 2.46	52 ± 3
Fe I 5506.779	18.37 ± 1.57	137.41 ± 2.02	55 ± 3
Na I 5889.950	20.63 ± 0.84	144.01 ± 1.13	337 ± 7
Na I 5895.924	20.69 ± 1.02	144.35 ± 1.42	204 ± 7
Fe I 6136.994	21.08 ± 3.63	133.25 ± 4.85	149 ± 7
Ca I 6162.170	19.44 ± 2.74	140.27 ± 4.07	65 ± 6
Fe I 6191.588	20.43 ± 2.43	139.27 ± 3.30	87 ± 7
Fe I 6230.723	20.26 ± 2.03	138.54 ± 2.75	92 ± 6
Fe I 6252.555	16.48 ± 2.40	140.87 ± 3.22	52 ± 5
Fe I 6393.601	21.92 ± 2.25	139.69 ± 3.10	65 ± 6
Fe I 6400.001	21.00 ± 2.89	127.53 ± 3.83	89 ± 7
Fe I 6430.846	17.43 ± 1.97	139.20 ± 2.53	84 ± 6
Fe I 6494.980	18.62 ± 1.14	130.75 ± 1.55	106 ± 5

H α 6562.760	18.91 ± 0.16	161.66 ± 0.20	2894 ± 9
Fe I 6677.987	23.21 ± 2.15	130.50 ± 2.70	71 ± 5
Ca II 8498.020	20.35 ± 0.13	144.80 ± 0.18	887 ± 4
Ca II 8542.090	20.13 ± 0.14	144.19 ± 0.20	847 ± 4
Ca II 8662.140	19.87 ± 0.17	142.89 ± 0.23	671 ± 4

Table A2. Secondary star emission lines in GK Vir. P is the hydrogen Paschen series. After measuring the radial velocity of a line, the spectra were shifted to remove the motion and averaged. The Equivalent widths were measured from this averaged spectrum.

Line	γ_{sec} (km/s)	K_{meas} (km/s)	Equivalent Width (mÅ)
H16 3703.853	-45.55 ± 2.07	200.01 ± 2.93	68 ± 3
H15 3711.971	-48.49 ± 1.83	203.33 ± 2.49	81 ± 2
Fe I 3719.935	-50.25 ± 1.55	197.94 ± 2.10	29 ± 2
H14 3721.948	-46.01 ± 1.21	204.48 ± 1.71	107 ± 2
H13 3734.372	-49.96 ± 1.01	199.31 ± 1.42	183 ± 2
Fe I 3737.131	-46.50 ± 1.00	199.97 ± 1.40	53 ± 2
H12 3750.152	-46.68 ± 0.73	203.38 ± 1.04	197 ± 2
H11 3770.634	-47.06 ± 0.49	203.61 ± 0.70	239 ± 2
H10 3797.910	-46.32 ± 0.39	202.72 ± 0.55	311 ± 2
He I 3819.761	-48.22 ± 0.73	201.68 ± 1.05	69 ± 2
H9 3835.397	-48.00 ± 0.32	204.37 ± 0.46	331 ± 2
Fe I 3856.371	-46.33 ± 1.11	204.48 ± 1.52	41 ± 2
H8 3889.055	-47.28 ± 0.21	203.86 ± 0.30	457 ± 2
Si I 3905.523	-45.96 ± 0.69	205.38 ± 0.97	58 ± 2
Ca II 3933.663	-46.67 ± 0.28	205.82 ± 0.39	208 ± 2
He I 3964.727	-48.70 ± 0.93	198.93 ± 1.36	44 ± 2
Ca II 3968.469	-46.78 ± 0.31	206.90 ± 0.40	158 ± 2
He ε 3970.074	-47.53 ± 0.20	205.75 ± 0.27	529 ± 2
He I 4026.189	-45.77 ± 0.49	204.70 ± 0.70	77 ± 1
Hδ 4101.735	-47.42 ± 0.18	205.81 ± 0.25	659 ± 3
He I 4143.759	-49.44 ± 0.87	198.33 ± 1.18	55 ± 2
Ca I 4226.728	-45.78 ± 1.44	209.03 ± 1.95	36 ± 2
Fe I 4232.726	-47.77 ± 1.15	201.03 ± 1.55	41 ± 2
Fe I 4266.964	-46.93 ± 0.92	198.87 ± 1.26	54 ± 2
Hγ 4340.465	-47.48 ± 0.16	207.11 ± 0.22	842 ± 3
Fe I 4351.544	-48.56 ± 1.04	201.36 ± 1.43	63 ± 2
He I 4387.928	-46.72 ± 0.61	197.68 ± 0.84	84 ± 2
He I 4471.480	-46.99 ± 0.32	202.90 ± 0.46	144 ± 2
Mg II 4481.130	-46.51 ± 0.72	201.59 ± 1.04	71 ± 2
Fe I 4549.467	-46.01 ± 1.05	201.43 ± 1.43	49 ± 2
He I 4713.146	-47.44 ± 0.49	204.45 ± 0.69	75 ± 2
Hβ 4861.327	-47.39 ± 0.16	208.67 ± 0.23	1406 ± 4
He I 4921.929	-48.30 ± 0.30	204.02 ± 0.43	149 ± 2
Fe II 4923.921	-47.35 ± 0.52	204.94 ± 0.73	80 ± 2
Fe I 4957.597	-46.94 ± 0.98	205.54 ± 1.44	59 ± 2
He I 5015.675	-48.93 ± 0.26	205.02 ± 0.37	197 ± 2
Fe II 5018.434	-48.60 ± 0.50	203.93 ± 0.73	105 ± 2
Mg I 5167.322	-49.24 ± 0.63	205.19 ± 0.90	90 ± 2
Fe I 5168.898	-45.00 ± 0.51	207.13 ± 0.73	112 ± 2
Mg I 5172.684	-46.67 ± 0.96	207.01 ± 1.41	127 ± 2
Mg I 5183.604	-48.44 ± 0.66	205.68 ± 0.99	136 ± 3
Fe I 5227.189	-46.44 ± 0.76	200.01 ± 1.10	70 ± 2
Fe I 5269.537	-48.88 ± 0.85	198.55 ± 1.27	92 ± 2
Fe II 5276.002	-48.15 ± 0.77	202.46 ± 1.11	80 ± 2
Fe II 5316.615	-46.43 ± 0.57	201.34 ± 0.82	102 ± 2
Fe I 5328.038	-47.10 ± 0.67	203.37 ± 0.99	126 ± 2
Fe I 5405.774	-48.88 ± 1.95	205.80 ± 1.59	51 ± 2
Fe I 5429.695	-46.80 ± 0.96	207.31 ± 1.43	73 ± 2
Fe I 5434.524	-48.12 ± 2.77	198.15 ± 3.37	25 ± 2
Fe I 5446.871	-45.26 ± 0.97	206.78 ± 1.41	53 ± 2
Fe I 5455.609	-46.39 ± 0.82	204.71 ± 1.20	62 ± 2
He I 5875.618	-47.07 ± 0.29	207.82 ± 0.41	623 ± 7
Na I 5889.950	-48.81 ± 1.07	211.58 ± 1.49	160 ± 8
Na I 5895.924	-49.29 ± 1.13	209.46 ± 1.59	124 ± 8
Fe I 6136.994	-45.82 ± 3.19	207.64 ± 3.19	112 ± 8
Ca I 6162.170	-49.04 ± 2.86	210.47 ± 2.27	31 ± 5
Fe I 6191.588	-48.29 ± 1.77	205.30 ± 2.30	47 ± 7
Mg II 6346.962	-45.17 ± 0.89	203.44 ± 1.21	123 ± 6
Fe I 6393.601	-46.88 ± 2.70	198.16 ± 3.22	50 ± 7
Fe I 6400.001	-46.92 ± 1.74	208.27 ± 2.57	57 ± 6
Fe II 6456.383	-46.43 ± 1.70	204.89 ± 2.21	125 ± 7
Ca I 6462.567	-47.03 ± 1.90	209.01 ± 2.58	37 ± 5
Fe I 6494.980	-46.55 ± 1.30	209.76 ± 1.74	56 ± 5

H α 6562.760	-46.77 ± 0.25	210.73 ± 0.33	4073 ± 13
He I 6678.149	-47.50 ± 0.51	206.26 ± 0.61	645 ± 7
He I 7065.188	-46.25 ± 0.54	205.69 ± 0.64	820 ± 7
He I 7281.349	-48.65 ± 0.64	202.81 ± 0.82	344 ± 8
O I 7771.944	-47.61 ± 0.61	203.64 ± 0.81	223 ± 5
O I 7774.166	-48.06 ± 1.39	202.84 ± 1.12	234 ± 5
O I 7775.388	-46.94 ± 1.55	204.89 ± 1.38	131 ± 5
Mg II 7896.368	-48.23 ± 0.90	202.55 ± 1.30	131 ± 7
Na I 8183.256	-49.93 ± 1.08	206.13 ± 1.62	74 ± 6
Na I 8194.824	-46.10 ± 1.46	206.74 ± 2.13	89 ± 7
Fe I 8327.056	-47.02 ± 1.04	200.82 ± 1.54	158 ± 8
C I 8335.150	-46.96 ± 0.69	207.21 ± 0.94	283 ± 7
O I 8446.359	-47.51 ± 0.73	206.06 ± 0.98	340 ± 9
Ca II 8498.020	-46.89 ± 0.19	207.18 ± 0.27	925 ± 9
Ca II 8542.090	-47.39 ± 0.15	207.64 ± 0.21	1322 ± 9
P14 8598.392	-48.88 ± 2.00	200.56 ± 2.78	256 ± 12
Ca II 8662.140	-47.65 ± 0.19	207.95 ± 0.29	901 ± 9
P13 8665.019	-45.51 ± 1.88	202.98 ± 2.68	489 ± 12
Fe I 8688.625	-48.01 ± 1.07	203.53 ± 1.66	176 ± 9
P12 8750.473	-44.68 ± 1.71	203.42 ± 2.50	719 ± 13
Mg I 8806.757	-46.67 ± 0.72	205.38 ± 0.99	244 ± 8
P11 8862.784	-45.69 ± 1.35	202.23 ± 1.93	1010 ± 13
Ca II 8912.070	-49.99 ± 0.78	202.51 ± 1.19	194 ± 9
Ca II 8927.360	-49.91 ± 0.76	202.22 ± 1.10	207 ± 9
P10 9014.911	-47.08 ± 0.66	201.91 ± 0.95	1337 ± 13
C I 9061.430	-46.69 ± 0.88	202.20 ± 1.12	638 ± 10
C I 9078.280	-46.30 ± 0.85	203.85 ± 1.08	255 ± 9
C I 9088.510	-47.30 ± 0.79	208.63 ± 1.07	378 ± 10
C I 9094.830	-45.99 ± 0.90	201.89 ± 1.19	385 ± 10
C I 9111.800	-48.71 ± 0.79	206.42 ± 1.01	281 ± 9
Fe I 9212.981	-48.42 ± 1.14	207.64 ± 1.67	212 ± 12
Mg II 9218.248	-46.67 ± 0.48	204.95 ± 0.70	493 ± 12
P9 9229.015	-49.80 ± 0.54	203.76 ± 0.78	2079 ± 20
Mg II 9244.266	-46.71 ± 0.63	203.53 ± 0.91	289 ± 11
C I 9405.730	-47.00 ± 0.77	208.83 ± 1.01	799 ± 19
P ϵ 9545.972	-47.40 ± 0.43	205.84 ± 0.62	2825 ± 26
C I 9620.800	-48.95 ± 1.00	204.99 ± 1.41	243 ± 15
C I 9658.440	-45.49 ± 0.99	208.87 ± 1.40	202 ± 18
P δ 10049.37	-48.12 ± 0.72	206.70 ± 0.65	3576 ± 60